

Dissipative ground-state preparation of a quantum spin chain on a trapped-ion quantum computer

Kazuhiro Seki,^{1,*} Yuta Kikuchi,^{2,3,†} Tomoya Hayata,^{4,3,5,‡} and Seiji Yunoki^{1,6,7,8,§}

¹*Quantum Computational Science Research Team, RIKEN Center for Quantum Computing (RQC), Saitama 351-0198, Japan*

²*Quantinuum K.K., Otemachi Financial City Grand Cube 3F, 1-9-2 Otemachi, Chiyoda-ku, Tokyo, Japan*

³*RIKEN Center for Interdisciplinary Theoretical and Mathematical Sciences (iTHEMS), RIKEN, Wako 351-0198, Japan*

⁴*Departments of Physics, Keio University School of Medicine, 4-1-1 Hiyoshi, Kanagawa 223-8521, Japan*

⁵*International Center for Elementary Particle Physics and The University of Tokyo, 7-3-1 Hongo, Bunkyo-ku, Tokyo 113-0033, Japan*

⁶*Computational Quantum Matter Research Team, RIKEN Center for Emergent Matter Science (CEMS), Wako, Saitama 351-0198, Japan*

⁷*Computational Materials Science Research Team, RIKEN Center for Computational Science (R-CCS), Kobe, Hyogo 650-0047, Japan*

⁸*Computational Condensed Matter Physics Laboratory,*

RIKEN Pioneering Research Institute (PRI), Saitama 351-0198, Japan

(Dated: January 14, 2026)

We demonstrate a dissipative protocol for ground-state preparation of a quantum spin chain on a trapped-ion quantum computer. As a first step, we derive a Kraus representation of a dissipation channel for the protocol recently proposed by Ding *et al.* [Phys. Rev. Res. **6**, 033147 (2024)] that still holds for arbitrary temporal discretization steps, extending the analysis beyond the Lindblad dynamics regime. The protocol guarantees that the fidelity with the ground state monotonically increases (or remains unchanged) under repeated applications of the channel to an arbitrary initial state, provided that the ground state is the unique steady state of the dissipation channel. Using this framework, we implement dissipative ground-state preparation of a transverse-field Ising chain for up to 19 spins on the trapped-ion quantum computer Reimei provided by Quantinuum. Despite the presence of hardware noise, the dynamics consistently converges to a low-energy state far away from the maximally mixed state even when the corresponding quantum circuits contain as many as 4110 entangling gates, demonstrating the intrinsic robustness of the protocol. By applying zero-noise extrapolation, the resulting energy expectation values are systematically improved to agree with noiseless simulations within statistical uncertainties.

I. INTRODUCTION

Estimating ground-state properties, such as energies, correlations, and entanglement, remains one of the most important and challenging tasks in quantum many-body physics [1]. A broad range of classical numerical methods, including exact diagonalization, variational Monte Carlo, quantum Monte Carlo, and density-matrix-renormalization group techniques, have been developed and benchmarked against paradigmatic models of strongly correlated systems, such as the Hubbard models [2–9] and the Heisenberg models [10–13]. These approaches have yielded valuable insights and cross-validations; however, accurately determining the ground-state properties of these systems remains classically intractable for large system sizes, especially in spatial dimensions greater than one. Recent quantum resource analyses suggest that ground-state energy estimation of the Hubbard and Heisenberg models via quantum phase estimation could offer one of the earliest demonstrations of practical quantum advantage once fault-tolerant quantum computers become available [14]. Ground-state energy estimation of molecules is likewise considered a promising target for demonstrating quantum advantage [15].

Despite such a promising assessment, quantum phase estimation will likely require fault-tolerant quantum computers to address classically intractable problems. In the meantime,

the variational quantum eigensolver (VQE) has been widely used to study ground-state properties of quantum many-body systems on noisy intermediate-scale quantum (NISQ) devices [16, 17]. Although VQE suffers from the notorious barren-plateau problem when optimizing variational parameters in deep circuits [18], it has nevertheless served as a cornerstone of quantum-classical hybrid algorithms. Recently, the quantum-selected configuration interaction (QSCI) method [19], also referred to as the sample-based quantum diagonalization (SQD) method [20], has been proposed as an alternative ground-state preparation protocol suitable for NISQ devices. The QSCI/SQD method avoids the variational-parameter optimization of VQE and simultaneously mitigates the measurement overhead associated with estimating energy expectation values. Following its initial proposal, several variants of the method have been developed [21–24] and implemented in the context of quantum-centric supercomputing [25] for large-scale electronic structure calculations using state-of-the-art quantum computers and classical supercomputers [20, 26, 27]. As with many emerging quantum algorithms, however, the superiority of QSCI/SQD over classical selected-CI approaches, such as the heat-bath CI method [28], remains under active discussion [26, 29], and further development of QSCI/SQD is ongoing.

The capability of quantum devices is growing rapidly. In particular, the ability to perform mid-circuit measurement and reset (MCMR) has not only enabled the simulation of open-quantum-system dynamics [30, 31], but also opened new avenues for exploring dissipation in optimization and state preparation [32, 33]. For example, MCMR makes it possible to prepare thermal Gibbs states on a quantum computer using Lindblad or open-quantum-system dynamics [34–39].

* kazuhiro.seki@riken.jp

† yuta.kikuchi@quantinuum.com

‡ hayata@keio.jp

§ yunoki@riken.jp

Beyond thermal-state preparation, dissipative protocols for ground-state preparation have recently attracted significant attention (see, e.g., Ref. [40] for a review). One example is the protocol demonstrated on a superconducting quantum processor by Mi *et al.* [41], in which quasiparticle excitations are released from the system to the environment, enabling efficient preparation of the ground state of one-dimensional (1D) transverse-field Ising models. More generally, Ding *et al.* proposed a protocol for preparing ground states of arbitrary quantum many-body Hamiltonians based on a completely positive and trace-preserving (CPTP) map specifically engineered to have the ground state as its unique steady state [42]. While this protocol is envisioned as an early-fault-tolerant quantum algorithm, it is important to examine its implementation and performance on currently available noisy quantum devices.

In this paper, we demonstrate a dissipative ground-state preparation protocol for a 1D transverse-field Ising model using the trapped-ion quantum computer Reimei [43]. First, we derive a Kraus representation of the dissipation channel that remains valid for arbitrarily large temporal-discretization steps. We then show that the fidelity with respect to the ground state is monotonically non-decreasing under repeated applications of the channel to an arbitrary initial state. We implement the protocol on Reimei to estimate the ground-state energy of the transverse-field Ising model for system sizes of up to 19 spins using a single ancilla qubit. By adopting zero-noise extrapolation (ZNE), we systematically obtain noise-mitigated energy expectation values that are consistent with noiseless simulations within statistical uncertainties.

The rest of the paper is organized as follows. In Sec. II, we review the dissipative ground-state preparation protocol proposed in Ref. [42] and reformulate it by deriving a Kraus representation of the corresponding CPTP map. In Sec. III, we present experimental results for dissipative ground-state preparation of a spin chain on a trapped-ion quantum device. In Sec. IV, we summarize our findings and discuss future perspectives. Additional details of the formalism, classical numerical results, and experimental results are provided in the Appendices.

II. METHOD

In this section, we review the dissipative ground-state preparation protocol proposed in Ref. [42]. We reformulate the protocol by deriving a Kraus representation of the corresponding dissipative channel and show, using the monotonicity of fidelity under CPTP maps, that the ground state is reached irrespective of the step size τ of the associated dilated time evolution $\hat{W}(\sqrt{\tau})$.

A. Dissipative ground state preparation

We aim to prepare the ground state of the Hamiltonian

$$\hat{H} = \sum_{i=0}^{d-1} E_i |E_i\rangle\langle E_i|, \quad (1)$$

where the eigenvalues satisfy $E_0 = E_1 = \dots = E_{g_0-1} < E_{g_0} \leq E_{g_0+1} \leq \dots \leq E_{d-1}$, with g_0 denoting the ground-state degeneracy. The Hilbert-space dimension is d , and $|E_0\rangle, |E_1\rangle, \dots, |E_{g_0-1}\rangle$ span the degenerate ground-state manifold. For notational convenience, we hereafter denote the ground state by $|E_0\rangle$; however, the following arguments apply equally to all degenerate ground states $|E_1\rangle, \dots, |E_{g_0-1}\rangle$. We assume that \hat{H} acts on a system of N qubits, implying $d = 2^N$.

We introduce a dissipative dynamics described by a CPTP map Γ_K , such that the ground state $|E_0\rangle\langle E_0|$ is its unique steady state:

$$\Gamma_K[|E_0\rangle\langle E_0|] = |E_0\rangle\langle E_0|. \quad (2)$$

Here, the subscript K denotes a jump operator that will be introduced below. To construct Γ_K , we introduce an ancilla qubit and define a dilated unitary acting on the combined ancilla-system Hilbert space (i.e., $N + 1$ qubits) as

$$\hat{W}(\sqrt{\tau}) = \exp(-i\hat{K}\sqrt{\tau}), \quad (3)$$

where τ is a positive real parameter, and \hat{K} is the dilated jump operator,

$$\hat{K} \equiv \begin{bmatrix} 0 & \hat{K}^\dagger \\ \hat{K} & 0 \end{bmatrix} = |1\rangle\langle 0|_a \otimes \hat{K} + |0\rangle\langle 1|_a \otimes \hat{K}^\dagger. \quad (4)$$

The jump operator \hat{K} , acting only on the system qubits, is designed to annihilate the ground state:

$$\hat{K}|E_0\rangle = 0. \quad (5)$$

An explicit construction of \hat{K} will be given in Sec. II B. We also note that \hat{K} annihilates the product state $|0\rangle\langle 0|_a \otimes |E_0\rangle\langle E_0|$; that is, $\hat{K}(|0\rangle\langle 0|_a \otimes |E_0\rangle\langle E_0|)\hat{K}^\dagger = 0$.

Suppose that the initial state of the total system is $|0\rangle\langle 0|_a \otimes \hat{\rho}$. The state evolved under $\hat{W}(\sqrt{\tau})$ is then

$$\hat{\sigma}(\tau) \equiv \hat{W}(\sqrt{\tau}) (|0\rangle\langle 0|_a \otimes \hat{\rho}) \hat{W}^\dagger(\sqrt{\tau}). \quad (6)$$

We define the dissipative channel as $\Gamma_K[\hat{\rho}] \equiv \text{Tr}_a[\hat{\sigma}(\tau)]$. By substituting the series expansion of $\hat{W}(\sqrt{\tau})$ into Eq. (6) and tracing out the ancilla, we obtain (see Appendix A for details)

$$\Gamma_K[\hat{\rho}] = \text{Tr}_a[\hat{\sigma}(\tau)] = \hat{C}\hat{\rho}\hat{C} + \tau\hat{K}\hat{S}_c\hat{\rho}\hat{S}_c\hat{K}^\dagger, \quad (7)$$

where

$$\hat{C} \equiv \cos \sqrt{\tau}\hat{K}^\dagger\hat{K} = \sum_{k=0}^{\infty} \frac{(-1)^k}{(2k)!} (\tau\hat{K}^\dagger\hat{K})^k, \quad (8)$$

$$\hat{S}_c \equiv \text{sinc} \sqrt{\tau}\hat{K}^\dagger\hat{K} = \sum_{k=0}^{\infty} \frac{(-1)^k}{(2k+1)!} (\tau\hat{K}^\dagger\hat{K})^k, \quad (9)$$

and $\sqrt{\hat{K}^\dagger\hat{K}}$ is well defined because $\hat{K}^\dagger\hat{K}$ is positive semidefinite. Introducing $\hat{M}_0 = \hat{C}$ and $\hat{M}_1 = -i\sqrt{\tau}\hat{K}\hat{S}_c$, Eq. (7) can be expressed in the standard Kraus form:

$$\Gamma_K[\hat{\rho}] = \hat{M}_0\hat{\rho}\hat{M}_0^\dagger + \hat{M}_1\hat{\rho}\hat{M}_1^\dagger \quad (10)$$

with the completeness relation

$$\hat{M}_0^\dagger \hat{M}_0 + \hat{M}_1^\dagger \hat{M}_1 = \cos^2 \sqrt{\tau \hat{K}^\dagger \hat{K}} + \sin^2 \sqrt{\tau \hat{K}^\dagger \hat{K}} = \hat{I}. \quad (11)$$

Thus, Eq. (7) provides a Kraus (Stinespring) representation of the channel Γ_K . Importantly, Eq. (2) holds for arbitrary τ as long as the jump operator satisfies $\hat{K}|E_0\rangle = 0$ [Eq. (5)]. As shown in Appendix A, the dissipative dynamics generated by Γ_K reduces to a Lindblad dynamics with jump operator \hat{K} in the limit $\tau \rightarrow 0$, up to $O(\tau^2)$.

We remark that the fidelity between the evolved state and the ground state is monotonically non-decreasing under the dissipative dynamics. For an arbitrary CPTP map \mathcal{E} and density operators $\hat{\rho}$ and $\hat{\sigma}$, the fidelity satisfies $F(\mathcal{E}[\hat{\rho}], \mathcal{E}[\hat{\sigma}]) \geq F(\hat{\rho}, \hat{\sigma})$, where the fidelity is defined as $F(\hat{\rho}, \hat{\sigma}) = \text{Tr} \sqrt{\sqrt{\hat{\sigma}} \hat{\rho} \sqrt{\hat{\sigma}}}$. Suppose that $\hat{\rho}^*$ is the unique steady state of \mathcal{E} , i.e., $\mathcal{E}[\hat{\rho}^*] = \hat{\rho}^*$. Then, $\mathcal{E}[\hat{\rho}] = \hat{\rho}$ holds if and only if $\hat{\rho} = \hat{\rho}^*$. Furthermore, $F(\mathcal{E}[\hat{\rho}], \mathcal{E}[\hat{\rho}^*]) = F(\mathcal{E}[\hat{\rho}], \hat{\rho}^*) \geq F(\hat{\rho}, \hat{\rho}^*)$, where equality holds only when $\hat{\rho} = \hat{\rho}^*$. Replacing $\hat{\rho}$ with $\mathcal{E}^m[\hat{\rho}]$, we obtain

$$F(\mathcal{E}^{m+1}[\hat{\rho}], \hat{\rho}^*) \geq F(\mathcal{E}^m[\hat{\rho}], \hat{\rho}^*), \quad (12)$$

indicating that $\mathcal{E}^m[\hat{\rho}]$ monotonically approaches the unique steady state $\hat{\rho}^*$ as m increases. In the present protocol, the CPTP map is the dissipative dynamics $\mathcal{E} = \Gamma_K$. Reference [42] shows that the ground state $\hat{\rho}^* = |E_0\rangle\langle E_0|$ is the unique steady state of Γ_K under appropriate assumptions on the jump operator \hat{K} and the initial state. Given the uniqueness of the steady state, the ground-state fidelity is therefore monotonically non-decreasing under successive applications of Γ_K . We note, however, that monotonicity of the fidelity does not necessarily imply monotonicity of the energy. Table I highlights the characteristics of the dissipative dynamics method for ground-state preparation in comparison with the imaginary-time evolution.

B. Jump operator and filter function

To obtain an explicit form of the jump operator, we write it as

$$\hat{K} = \sum_{i,j=0}^{d-1} \tilde{f}(E_i - E_j) |E_i\rangle\langle E_i| \hat{A} |E_j\rangle\langle E_j|, \quad (13)$$

where \hat{A} is an arbitrary operator and \tilde{f} is a filter function that satisfies

$$\tilde{f}(\omega) = 0 \quad \text{for } \omega > 0 \quad (14)$$

so that \hat{K} induces no energy-increasing transitions. Although we assume that \hat{A} is Hermitian, the jump operator \hat{K} is in general non-Hermitian.

For convenience in implementation, we rewrite the jump operator in the form of an operator Fourier transform (OFT) [35]:

$$\hat{K} = \int_{-\infty}^{\infty} ds f(s) \hat{A}(s) \quad \text{with} \quad \hat{A}(s) = e^{i\hat{H}s} \hat{A} e^{-i\hat{H}s}. \quad (15)$$

The filter function in the frequency domain, $\tilde{f}(\omega)$, is related to its time-domain representation $f(s)$ via

$$f(s) = \frac{1}{2\pi} \int_{-\infty}^{\infty} d\omega \tilde{f}(\omega) e^{-i\omega s}. \quad (16)$$

C. Interaction between ancilla and system

To construct the Stinespring dilation unitary $\hat{W}(\sqrt{\tau})$ as a quantum circuit, we rewrite the interaction operator \hat{K} between the system and the ancilla in Eq. (4) as

$$\hat{K} = \begin{bmatrix} 0 & \text{Re}\hat{K} - i\text{Im}\hat{K} \\ \text{Re}\hat{K} + i\text{Im}\hat{K} & 0 \end{bmatrix} = \hat{X}_a \otimes \text{Re}\hat{K} + \hat{Y}_a \otimes \text{Im}\hat{K}, \quad (17)$$

where \hat{X}_a and \hat{Y}_a are Pauli X and Y operators acting on the ancilla qubit, and $\text{Re}\hat{K}$ and $i\text{Im}\hat{K}$ denote the Hermitian and skew-Hermitian parts of \hat{K} :

$$\text{Re}\hat{K} \equiv \frac{\hat{K} + \hat{K}^\dagger}{2} = \int_{-\infty}^{\infty} ds \text{Re}f(s) \hat{A}(s), \quad (18)$$

$$\text{Im}\hat{K} \equiv \frac{\hat{K} - \hat{K}^\dagger}{2i} = \int_{-\infty}^{\infty} ds \text{Im}f(s) \hat{A}(s). \quad (19)$$

Using $\text{Re}f(s) = |f(s)| \cos \varphi(s)$ and $\text{Im}f(s) = |f(s)| \sin \varphi(s)$ with $\varphi(s) = \arg f(s)$, we obtain

$$\hat{K} = \int_{-\infty}^{\infty} ds |f(s)| (\cos \varphi(s) \hat{X}_a + \sin \varphi(s) \hat{Y}_a) \otimes \hat{A}(s). \quad (20)$$

For convenience, we express the single-qubit operator acting on the ancilla in Eq. (20) as

$$\hat{P}(s) \equiv \cos \varphi(s) \hat{X}_a + \sin \varphi(s) \hat{Y}_a = \hat{R}_{Z_a}(\varphi(s)) \hat{X}_a \hat{R}_{Z_a}^\dagger(\varphi(s)), \quad (21)$$

where $\hat{R}_{Z_a}(\varphi) = e^{-i\varphi \hat{Z}_a/2}$ is a single-qubit Z -rotation acting on the ancilla. The dilated unitary operator can then be expressed as

$$\hat{W}(\sqrt{\tau}) = \exp \left[-i \sqrt{\tau} \int_{-\infty}^{\infty} ds |f(s)| \hat{P}(s) \otimes \hat{A}(s) \right]. \quad (22)$$

D. Truncation and discretization of the OFT

We implement the unitary $\hat{W}(\sqrt{\tau})$ by truncating and discretizing the time integral of the OFT in Eq. (15), and by decomposing the resulting exponential using suitable Trotter steps. As we shall see later, we choose $f(s)$ such that $|f(s)|$ decays exponentially in $|s|$. We may therefore truncate the integral to the finite interval $[-S_s, S_s]$ and discretize it as

$$\hat{K} \approx \sum_{l=-M_s}^{M_s} \Delta_s |f(s_l)| \hat{P}(s_l) \otimes \hat{A}(s_l), \quad (23)$$

TABLE I. Comparison between the dissipative dynamics method and the imaginary-time evolution for ground-state preparation.

Method	Operations	Monotonicity	Time to convergence
Dissipative dynamics	Unitary + Partial trace	Non-decreasing fidelity in time	$(\text{Liouvillian gap})^{-1}$
Imaginary-time evolution	Unitary + Post selection	Non-increasing energy in time	$(\text{Energy gap})^{-1}$

where $s_l = l\Delta_s$ ($l = -M_s, -M_s + 1, \dots, M_s$), and $\Delta_s = S_s/M_s$ with M_s being a positive integer. Under this time discretization, we use the second-order Trotter formula (with respect to Δ_s) to approximate the unitary as

$$\hat{W}(\sqrt{\tau}) \approx \prod_{l=-M_s}^{M_s} \hat{U}(s_l) \prod_{l=M_s}^{-M_s} \hat{U}(s_l), \quad (24)$$

where

$$\begin{aligned} \hat{U}(s_l) &= \exp \left[-i \frac{\sqrt{\tau}}{2} \Delta_s |f(s_l)| \hat{P}(s_l) \otimes \hat{A}(s_l) \right] \\ &\stackrel{\text{Eq. (21)}}{=} \hat{V}^\dagger(s_l) \exp \left[-i \frac{\sqrt{\tau}}{2} \Delta_s |f(s_l)| \hat{X}_a \otimes \hat{A} \right] \hat{V}(s_l) \end{aligned} \quad (25)$$

with

$$\hat{V}(s_l) = \hat{R}_{Z_a}^\dagger(\varphi(s_l)) \otimes e^{-i\hat{H}s_l}. \quad (26)$$

Using $s_{l+1} = s_l + \Delta_s$, we further obtain

$$\hat{V}^\dagger(s_{l+1}) \hat{V}(s_l) = \hat{R}_{Z_a}(\varphi(s_{l+1})) \hat{R}_{Z_a}^\dagger(\varphi(s_l)) \otimes e^{i\hat{H}\Delta_s}. \quad (27)$$

This shows that, in two consecutive applications $\hat{U}(s_{l+1})\hat{U}(s_l)$, the net operation on the system is the short-time evolution $\hat{I} \otimes e^{i\hat{H}\Delta_s}$ except at the first and last time slices.

At the boundaries of the Trotterized sequence in Eq. (24) (i.e., at $l = -M_s$), $\hat{V}(s_{-M_s})$ and $\hat{V}^\dagger(s_{-M_s})$ introduce coherent evolutions $\hat{I} \otimes e^{i\hat{H}S_s}$ and $\hat{I} \otimes e^{-i\hat{H}S_s}$ on the system. These operations cancel when $\hat{W}(\sqrt{\tau})$ is applied repeatedly, except during the very first and last applications. Since $\hat{I} \otimes e^{i\hat{H}S_s}$ merely alters the initial state, and $\hat{I} \otimes e^{-i\hat{H}S_s}$ produces only an overall phase on the ground state of \hat{H} , we remove these endpoint coherent evolutions from the first and last segments of the Trotterized implementation, following Ref. [42].

III. QUANTUM EXPERIMENTS

A. Hamiltonian

To demonstrate the protocol described above, we consider the 1D transverse-field Ising model,

$$\hat{H} = J \sum_{i=0}^{N-2} \hat{Z}_i \hat{Z}_{i+1} + B_X \sum_{i=0}^{N-1} \hat{X}_i, \quad (28)$$

where N is the number of system qubits, and J and B_X denote the exchange and transverse-field strengths, respectively. We study systems of sizes $N = 4, 6$, and 19 under open boundary conditions, using the parameters $J = -1$ and $B_X = -1.2$.

B. Jump operator and filter function

The choice of the jump operator plays a crucial role in determining the convergence behavior of the dissipative dynamics toward the steady state [44]. For simplicity of implementation, we follow Ref. [42] and choose the jump operator to be $\hat{A} = \hat{Z}_0$, i.e., the Pauli-Z operator acting on the first qubit of the spin chain. With this choice, the interaction term between the ancilla and the system, $e^{-i\frac{\sqrt{\tau}}{2}\Delta_s|f(s_l)|\hat{X}_a \otimes \hat{A}}$ in Eq. (25), can be implemented straightforwardly using elementary quantum gates.

As a filter function $\tilde{f}(\omega)$, we employ

$$\tilde{f}(\omega) = n_F(\beta(\omega - b)) - n_F(\beta(\omega - a)), \quad (29)$$

where $n_F(x) = 1/(e^x + 1)$ is the Fermi-Dirac distribution function, and a , b , and β are free parameters. Throughout this work, we assume $a < b < 0$ and $\beta > 0$. To ensure that the dissipative dynamics generated by the jump operator \hat{K} prepares the ground state of the Hamiltonian, the filter function must have support only on the negative-frequency side [see Eq. (14)], so that \hat{K} suppresses transitions to higher-energy states. In the limit $\beta \rightarrow \infty$, the function in Eq. (29) approaches an ideal rectangular window and exactly satisfies Eq. (14). For finite β , however, the edges of the window are rounded: $\tilde{f}(\omega) \approx 1$ for $a + \frac{1}{\beta} \lesssim \omega \lesssim b - \frac{1}{\beta}$ and $\tilde{f}(\omega) \approx 0$ for $\omega \lesssim a - \frac{1}{\beta}$ or $b + \frac{1}{\beta} \lesssim \omega$. We refer to this $O(1/\beta)$ rounding relative to the rectangular window as the genuine broadening of the filter function.

The Fourier transform of the filter function is given by

$$f(s) = e^{-i\frac{b+a}{2}s} \frac{\sin\left(\frac{b-a}{2}s\right)}{\beta \sinh\left(\frac{\pi}{\beta}s\right)} \quad (30)$$

with the normalization $f(0) = (b - a)/2\pi$ (see Appendix B for a detailed derivation). For finite values of β , the modulus $|f(s)|$ decays exponentially with increasing $|s|$ due to the hyperbolic sine function $\sinh\left(\frac{\pi}{\beta}s\right)$ in the denominator. In contrast, the sine function in the numerator leads to zeros at $s = 2\pi n/(b-a)$ for any nonzero integer n . As a guideline, the parameters β , b , and a can be chosen as follows. The scale $1/\beta$ should be on the order of the excitation gap of the Hamiltonian; b should be a negative value on the order of $1/\beta$; and a should be a negative value on the order of the spectral radius of the Hamiltonian. In the quantum experiments presented in this work, we set $\beta = 8/\Delta$, $b = -2/\beta = \Delta/4$, and $a = -2|E_0|$, where $\Delta = E_{g_0} - E_0$ denotes the excitation gap. Because the system sizes considered here are sufficiently small, we evaluate E_0 and $E_{g_0} = E_1$ using exact diagonalization. Note that $|a| = 2|E_0|$ corresponds to twice the spectral radius of \hat{H} . Numerical examples of the filter functions $\tilde{f}(\omega)$ and $f(s)$ for the

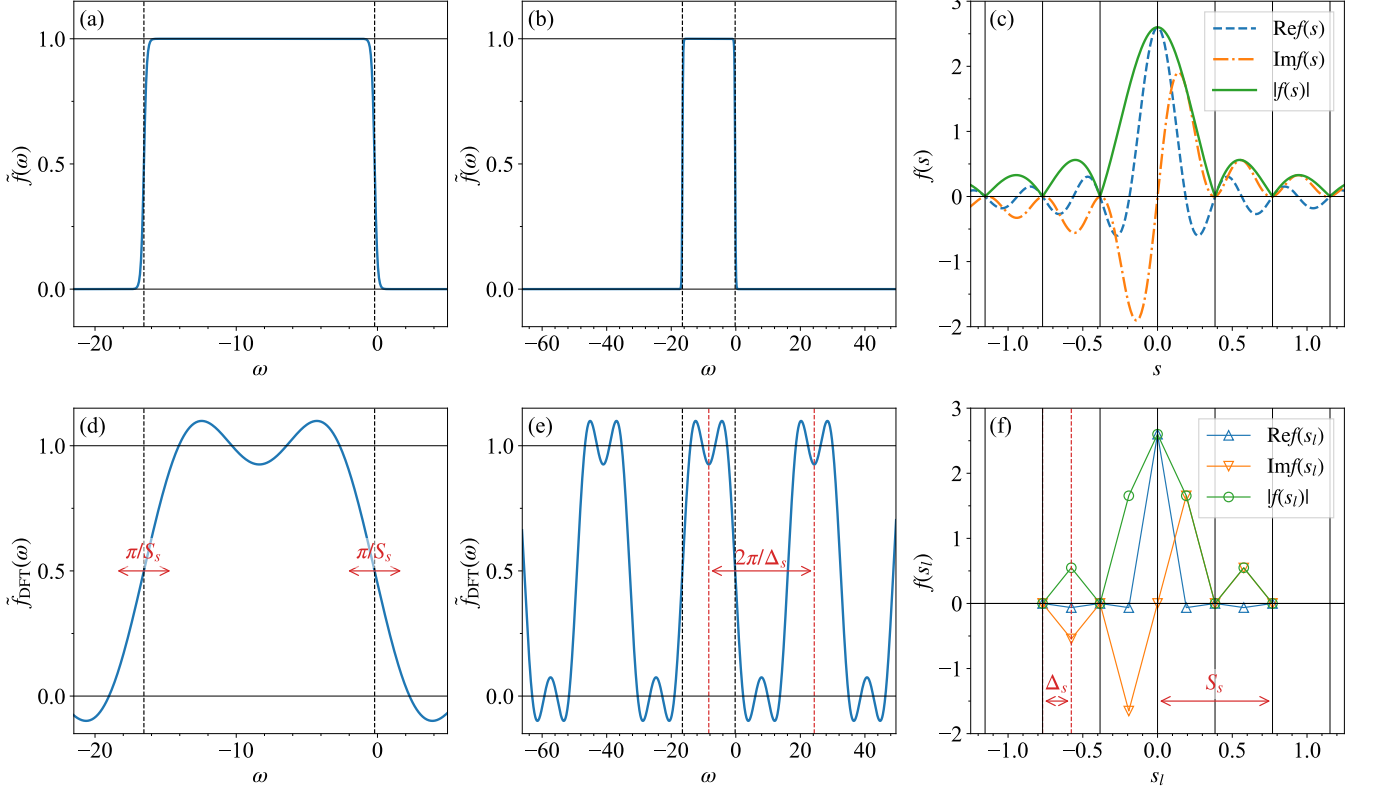


FIG. 1. (a) Example of the filter function $\tilde{f}(\omega)$ in the frequency domain. The dashed vertical lines indicate $\omega = a$ and $\omega = b$ with $a < b < 0$. (b) Same as (a), but shown over a wider frequency range. (c) Fourier transform $f(s)$ of the filter function $\tilde{f}(\omega)$. The quantities $|f(s)|$, $\text{Ref}(s)$, and $\text{Im}f(s)$ are shown as solid, dashed, and dash-dotted curves, respectively. The solid vertical lines mark $s = 2\pi n/(b - a)$ for integer n , where $f(s) = 0$ except at $s = 0$. (d-f) Same as (a-c), but with time discretization. In (d), the red arrows at $\omega = a$ and $\omega = b$ indicate the edge broadening of width π/S_s , arising from truncation of the time-integration range. In (e), the red arrow indicates the aliasing period $2\pi/\Delta_s$, corresponding to the discrete sampling points of $f(s_l)$ shown in (f). In (f), the large and small arrows indicate the time-discretization parameters S_s and Δ_s , respectively. The discretized values $f(s_l)$ shown in (f) are used in the quantum experiments for the $N = 6$ system.

$N = 6$ system are shown in Figs. 1(a) and 1(b), and Fig. 1(c), respectively.

C. Truncation and discretization of the OFT

As described in Sec. II D, implementing $\hat{W}(\sqrt{\tau})$ in Eq. (22) on a quantum computer requires discretizing the associated time integral as in Eqs. (23) and (24). We truncate the integration range using $S_s = 4\pi/(b-a)$ and discretize it with $M_s = 4$, giving $\Delta_s = S_s/M_s = \pi/(b-a)$. These values are chosen to ensure that the resulting circuit remains feasible within our available quantum computational resources. The discrete Fourier transform (DFT) of $f(s)$, $\tilde{f}_{\text{DFT}}(\omega) \equiv \sum_{l=-M_s}^{M_s} \Delta_s f(s_l) e^{i\omega s_l}$, and the discretized values $f(s_l)$ for $|s_l| \leq S_s$ are shown in Figs. 1(d) and 1(e), and Fig. 1(f), respectively. Below, we describe how the DFT-based filter function $\tilde{f}_{\text{DFT}}(\omega)$ behaves as a consequence of truncating and discretizing $f(s)$.

The truncation of the integration range (S_s) in $f(s_l)$ induces oscillations in $\tilde{f}_{\text{DFT}}(\omega)$ and effectively broadens the edges of $\tilde{f}_{\text{DFT}}(\omega)$ at $\omega = a$ and $\omega = b$. A nonvanishing value of $\tilde{f}(\omega)$ at $\omega > 0$, i.e., a violation of Eq. (14), implies that the jump op-

erator \hat{K} contains energy-increasing transitions, in which case the ground state is no longer the steady state. This leads to a systematic error even in noiseless simulations. As shown in Fig. 1(d), the broadening of the edges caused by the truncation can be estimated as $\sim \pi/S_s$, which is larger than the intrinsic broadening $1/\beta$ of the exact filter function in Eq. (29). This observation suggests choosing $S_s = O(\beta)$ in order to capture the genuine broadening of the filter function. Indeed, Appendix C 2 shows that the truncation error decays as $e^{-\pi S_s/\beta}$.

The discretization of the integral (Δ_s) in $f(s)$ induces aliasing in $\tilde{f}_{\text{DFT}}(\omega)$ with a period $\omega_{\text{alias}} = 2\pi/\Delta_s$. As observed in Fig. 1(e), the separation between the right edge of the filter function around the support of the original filter and the left edge of the spurious right-adjacent copy is approximately $\omega_{\text{alias}} - (b - a)$, where we ignore the broadening of the edges. For the present choice of Δ_s , we have $\omega_{\text{alias}} = 2(b - a)$, and thus the separation is about $b - a$, which is nearly twice the spectral radius of \hat{H} . This implies that the error due to discretization should be insignificant. As shown in Appendix C 1, the discretization error decays as $e^{-\beta(\omega_{\text{alias}} - 2\|\hat{H}\|)}$.

D. Discrete time evolution

We consider a single step of the discrete-time evolution,

$$\hat{\rho}(m+1) = \Gamma_H \circ \Gamma_K \circ \Gamma_H[\hat{\rho}(m)], \quad (31)$$

where

$$\Gamma_H[\hat{\rho}] = [e^{-i\hat{H}\Delta_t}]^{N_t/2} \hat{\rho} [e^{i\hat{H}\Delta_t}]^{N_t/2}. \quad (32)$$

implements a coherent unitary time evolution under the transverse-field Ising Hamiltonian for a duration $t/2 = N_t \Delta_t/2$. We interleave dissipative and coherent evolution in order to accelerate convergence toward the ground state, as observed in Refs. [37, 42, 45]. The short-time propagator $e^{-i\hat{H}\Delta_t}$ for a small time step Δ_t is approximated using the second-order Trotter formula, $e^{-i\hat{H}\Delta_t} = e^{-i\hat{H}_X\Delta_t/2} e^{-i\hat{H}_{ZZ}\Delta_t} e^{-i\hat{H}_X\Delta_t/2} + O(\Delta_t^3)$, where \hat{H}_{ZZ} and \hat{H}_X denote the Ising and transverse-field terms of the Hamiltonian \hat{H} in Eq. (28), respectively. An analogous Trotterization is applied to the short-time evolution $e^{i\hat{H}\Delta_t}$ that appears in Γ_K [see Eqs. (6), (7), (24), and (27)].

E. Experimental details

We use Quantinuum's trapped-ion quantum computer Reimeei [43] to evaluate the energy expectation value along the dissipative evolution [46]. At the time of the experiments, the Reimeei system consisted of 20 qubits and natively supported single-qubit rotation gates and a parametrized two-qubit gate $R_{ZZ}(\alpha) = e^{-\frac{1}{2}i\pi\alpha\hat{Z}_i\hat{Z}_j}$, where α is a real-valued parameter. The native two-qubit gate could be applied to arbitrary pairs of qubits. The average infidelities of the single-qubit and two-qubit gates were approximately 0.004% and 0.14%, respectively, and the average state-preparation-and-measurement (SPAM) error was around 0.35%. All quantum circuits used in the experiments were compiled using TKET [47].

F. Energy expectation values

Figure 2 shows the quantum circuit used to estimate the expectation value $\text{Tr}[\hat{\rho}(m)\hat{O}]$ of an observable \hat{O} . The first qubit serves as the ancilla, and the remaining six qubits represent the system. The initial state is prepared as $|0\rangle\langle 0|_a \otimes \hat{\rho}(0)$. The gray box denotes the coherent unitary evolution of the system under the Hamiltonian \hat{H} , while the blue box represents the dilated unitary $\hat{W}(\sqrt{\tau})$. The reset of the ancilla qubit, which discards information about the measurement outcome, effectively implements the partial trace over the ancilla, provided that a sufficiently large number of shots is taken. The white box corresponds to a basis rotation to measure the observable \hat{O} , after which the system qubits are measured in the computational basis. For example, the basis rotation is the identity when measuring $\hat{O} = \hat{Z}_i\hat{Z}_{i+1}$, whereas it consists of Hadamard gates when measuring $\hat{O} = \hat{X}_i$. The total number of SPAM

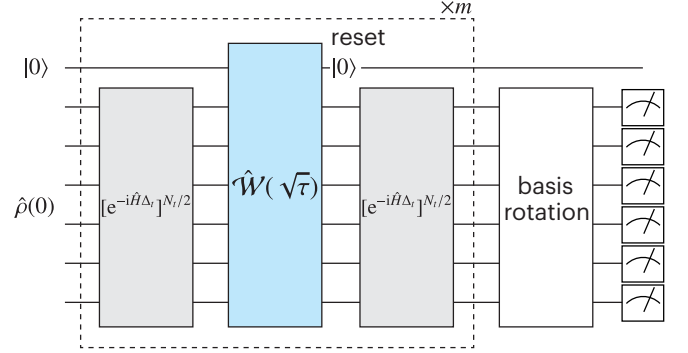


FIG. 2. Quantum circuit used to estimate the expectation value $\text{Tr}[\hat{\rho}(m)\hat{O}]$. The topmost qubit, initialized in the state $|0\rangle$, serves as the ancilla, while the remaining qubits, initialized in the state $\hat{\rho}(0)$, serve as the system qubits.

operations in the circuit, including qubit initializations and resets, is $N_{\text{SPAM}} = m + 2N + 1$, where m accounts for the resets of the ancilla qubit, $N + 1$ corresponds to the initializations, and N arises from the final measurements of the system qubits.

Figure 3 shows the energy expectation value

$$E(m) = \text{Tr}[\hat{\rho}(m)\hat{H}] \quad (33)$$

of the transverse-field Ising model as a function of the time step m . We set the parameters of the dynamics to $\tau = 4$, $\Delta_t = 0.25$, and $N_t = 4$. The choice $\tau = 4$ is motivated by noiseless simulations for the $N = 6$ system, where it yields the fastest convergence to the steady state among the values of τ that we examined (see Appendix D). The initial state is prepared as the product state of Pauli- Y eigenstates, $\hat{\rho}(0) = \prod_i [(\hat{I}_i + \hat{Y}_i)/2]$. Since the Hamiltonian contains only Pauli- X and Z operators, the corresponding energy expectation value at $m = 0$ is $E(0) = \text{Tr}[\hat{\rho}(0)\hat{H}] = 0$. Experiments are performed on Reimeei, and noiseless simulations are carried out using the Aer simulator of Qiskit [48]. We also include results obtained from the noisy Reimeei emulator (denoted as Reimeei-E), which closely reproduces the behavior of the hardware. The number of measurement shots is set to $N_{\text{shots}} = 100$ for Reimeei and Reimeei-E, and $N_{\text{shots}} = 1000$ for the noiseless Aer simulator. Using a single ancilla qubit, the total number of qubits required in the experiments is $N + 1$.

First, the results obtained from Reimeei-E agree well with the hardware results of Reimeei, remaining within a few standard deviations for both $N = 4$ and $N = 6$, as shown in Fig. 3. The number of native two-qubit gates (i.e., R_{ZZ} gates) scales as $N_{2Q} = 57m$ for $N = 4$ and $N_{2Q} = 79m$ for $N = 6$. Thus, the largest circuits at $m = 20$ contain 1140 and 1580 R_{ZZ} gates for $N = 4$ and $N = 6$, respectively. Given the two-qubit gate fidelity of $1 - 1.4 \times 10^{-3} = 0.9986$, a naive estimate of the overall circuit fidelity at $m = 20$ would be $(0.9986)^{1140} \approx 0.2$ for $N = 4$ and $(0.9986)^{1580} \approx 0.11$ for $N = 6$. Because \hat{H} is traceless, the energy expectation value of the completely mixed state \hat{I}/d is $\text{Tr}[\hat{H}]/d = 0$. If we assume that the noisy state at $m = 20$ is described by a mixture of the ground state and the completely mixed state—with the former contributing

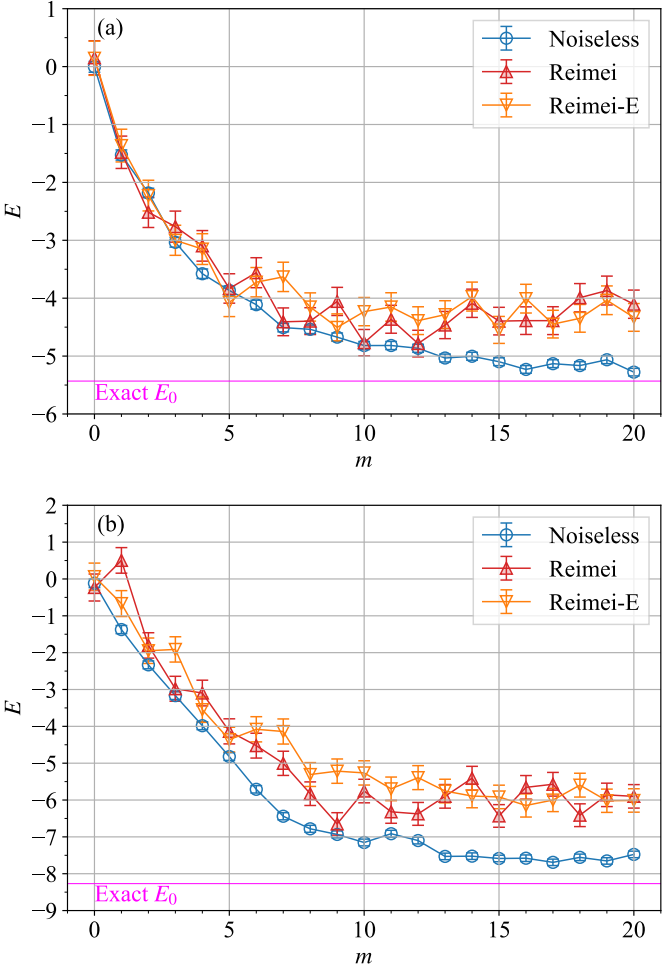


FIG. 3. Energy $E(m)$ as a function of the time steps m for (a) $N = 4$ and (b) $N = 6$. The parameters $J = -1$ and $B_X = -1.2$ are used for the transverse-field Ising model in both cases. Blue circles, red filled triangles, and orange inverted triangles show results from noiseless simulations (Noiseless), the noisy emulator (Reimei-E), and the quantum hardware (Reimei), respectively. For each data point, Noiseless results are obtained using 1000 measurement shots, whereas Reimei and Reimei-E results are obtained using 100 measurement shots. Error bars indicate the standard deviations. The exact ground-state energy E_0 is shown as a magenta horizontal line.

a fraction of 0.2 or 0.11 (as in the depolarizing channel)—then we would expect $E(m = 20) = \text{Tr}[\hat{\rho}(20)\hat{H}] \sim 0.2 \times E_0$ or $0.11 \times E_0$, where E_0 denotes the exact ground-state energy. However, the experimental signals in Fig. 3 are significantly better than these naive estimates. As discussed above, the dissipative channel Γ_K has the ground state as the steady state of the dynamical map, which suggests an intrinsic robustness of the protocol to noise. Indeed, we observe that a steady state persists even in the presence of non-negligible hardware noise. Although noise may shift the steady state from the ideal noiseless one $\hat{\rho}^*$ to another higher-energy state $\hat{\rho}_{\text{noisy}}^*$, this noisy state is not the completely mixed state $\hat{\rho}_{\text{noisy}}^* \neq \hat{I}/d$, as evidenced by Fig. 3, where the energy expectation values

converge to finite values rather than zero. Thus, a reasonably good approximation of the ground state can still be prepared despite the presence of noise. A related analysis of robustness can be found in Ref. [37]. We also note that even the noiseless simulation does not converge exactly to the true ground-state energy due to systematic discretization errors.

G. Zero-noise extrapolation

We now assess the ability of ZNE to mitigate errors. We adopt the gate-folding method applied to the native two-qubit gates, i.e., the $R_{ZZ}(\theta)$ gates. In this method, each $R_{ZZ}(\theta)$ gate in a compiled circuit is replaced by

$$R_{ZZ}(\theta) \mapsto [R_{ZZ}(\theta)R_{ZZ}(-\theta)]^{\frac{G-1}{2}} R_{ZZ}(\theta), \quad (34)$$

where the noise-scaling factor G is an odd integer. Specifically, we consider circuits with $G = 1, 3$, and 5 , where $G = 1$ corresponds to the original circuit. We first compile the $G = 1$ circuit for the target device using the Pytket SDK [49] with the most aggressive optimization setting `optimisation_level=3`. For $G = 3$ and 5 , we then replace each R_{ZZ} gate in the compiled circuit according to Eq. (34). For extrapolation, we employ both linear and exponential fits of the expectation values as a function of G . The fitting functions take the form $\tilde{a}G + \tilde{b}$ (linear) and $\tilde{a} \exp(\tilde{b}G)$ (exponential), where \tilde{a} and \tilde{b} are fitting parameters. Energy expectation values are then estimated by extrapolating the data at two points ($G = 1$ and 3) using the linear fit, or at three points ($G = 1, 3$, and 5) using the exponential fit, to the zero-noise limit $G \rightarrow 0$.

Figure 4 shows the ZNE results for the $N = 6$ system, using the same model parameters as in Fig. 3. Noisy data for $G = 1, 3$, and 5 are obtained on Reimei, with $N_{\text{shots}} = 100$ for each value of m and G . We note that the results for $G = 1$ in Fig. 4 are the same as those shown in Fig. 3(b). The number of R_{ZZ} gates in the circuit at m th time step scales as $N_{2Q} = 79Gm$. At $m = 0$, ZNE data are not shown because $N_{2Q}(m = 0) = 0$. For $m \geq 15$, ZNE with the exponential fit exhibits better agreement with the noiseless results than the linear fit, although in most cases the two extrapolation schemes agree within statistical uncertainties. At the largest time step $m = 20$, the relative error of the noisy $G = 1$ data, defined as $|1 - E_{G=1}(m)/E_{\text{Noiseless}}(m)|$, is approximately 0.3, where the subscripts (“ $G = 1$ ” and “Noiseless”) match the legend labels used in Fig. 4. This error is successfully eliminated by the exponential ZNE extrapolation. Details of the fitting procedures are provided in Appendix E.

Figure 5 shows the ZNE results for the $N = 19$ system, using the same model parameters as in Fig. 4. Noisy data for $G = 1, 3$, and 5 are obtained on Reimei for time steps up to $m \leq 30$, with $N_{\text{shots}} = 100$ for each value of m and G . The number of R_{ZZ} gates in the circuit at time step m scales as $N_{2Q} = 137Gm$, and thus the largest circuits at $m = 30$ contain 4110, 12330, and 20550 R_{ZZ} gates for $G = 1, 3$, and 5 , respectively. Although the discrepancy between the exact ground-state energy E_0 and the noiseless simulation results is more pronounced than in the $N = 6$ case, the overall behavior remains qualitatively similar. The ZNE extrapolation using

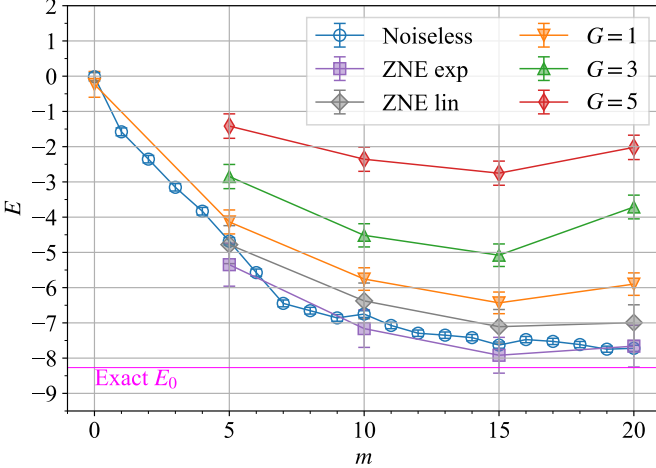


FIG. 4. Energy $E(m)$ as a function of the time step m for the $N = 6$ transverse-field Ising model with parameters $J = -1$ and $B_X = -1.2$. Results for noise-scaling factors $G = 1, 3$, and 5 are obtained on Reimei. For each data point, Noiseless results use 1000 measurement shots, whereas the Reimei results for $G = 1, 3$, and 5 use 100 measurement shots. “ZNE exp” and “ZNE lin” denote the ZNE estimates obtained via exponential and linear extrapolations, respectively. Error bars indicate the standard deviations and, for the ZNE exp and ZNE lin data, also include the uncertainty associated with the extrapolation. The exact ground-state energy E_0 is indicated by the magenta horizontal line.

the exponential fit shows consistently better agreement with the noiseless results than the linear fit, particularly at $m = 20$ and 30 . Even at $m = 30$, the ZNE estimate agrees with the noiseless value within two standard deviations, although the agreement is less evident than at earlier times ($m = 10$ and 20). At $m = 30$, the relative error in the noisy $G = 1$ data, quantified as $|1 - E_{G=1}(m)/E_{\text{Noiseless}}(m)| \sim 0.5$, is reduced by approximately a factor of three when applying ZNE with the exponential fit: $|1 - E_{\text{ZNE exp}}(m)/E_{\text{Noiseless}}(m)| \sim 0.15$. Details of the fitting procedure are provided in Appendix E.

Due to the limitation on the maximum number of quantum gate operations allowed per circuit on Reimei and Reimei-E, we were unable to perform ZNE—particularly for $G = 3$ and 5 —for time steps $m \geq 40$. Instead, we carry out noisy simulations using Reimei-E with $G = 1$ for $m \geq 30$. The results are shown as orange open triangles in Fig. 5. Remarkably, even at $m = 100$, where the circuit contains $N_{2Q} = 13700 R_{ZZ}$ gates, we still observe a nonzero energy expectation value. This further demonstrates the robustness of the dissipative ground-state preparation protocol against noise.

IV. SUMMARY AND DISCUSSION

We have demonstrated a dissipative ground-state preparation protocol for a one-dimensional transverse-field Ising model on the trapped-ion quantum computer Reimei. To this end, we derived a Kraus representation of the corresponding

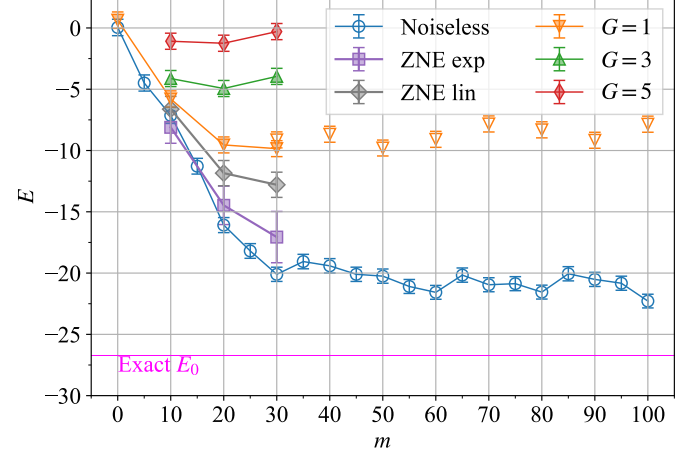


FIG. 5. Energy $E(m)$ as a function of the time step m for the $N = 19$ transverse-field Ising model with parameters $J = -1$ and $B_X = -1.2$. Results for noise-scaling factors $G = 1, 3$, and 5 for $m \leq 30$ are obtained on Reimei. For comparison, results obtained with Reimei-E for $G = 1$ at $m \geq 30$ are also shown as orange open triangles. For each data point, Noiseless results use 1000 measurement shots, whereas the Reimei results for $G = 1, 3$, and 5 and the Reimei-E results for $G = 1$ at $m \geq 30$ use 100 measurement shots. “ZNE exp” and “ZNE lin” denote the ZNE estimates obtained via exponential and linear extrapolations, respectively. Error bars indicate the standard deviations and, for the ZNE exp and ZNE lin data, also include the uncertainty associated with the extrapolation. The exact ground-state energy E_0 is indicated by the magenta horizontal line.

dissipation channel and showed that the fidelity with respect to the ground state is monotonically nondecreasing under successive applications of the channel to any initial state.

Specifically, we applied the protocol to estimate the ground-state energy of the transverse-field Ising model for system sizes up to $N = 19$ sites. To implement the protocol, we used $N + 1$ qubits of the trapped-ion quantum computer, where the additional qubit serves as the ancilla required to realize the dissipative dynamics via the Stinespring dilation unitary. In the presence of hardware noise, the measured energy expectation values did not converge to those obtained from noiseless simulations. To address this deviation, we employed ZNE and obtained energy estimates that agree with the noiseless results within statistical uncertainties. We found that ZNE with the exponential extrapolation yields better agreement with the noiseless results than linear extrapolation. For the $N = 6$ system, the errors are almost completely eliminated by ZNE, whereas for the $N = 19$ system, the errors at the largest time step are reduced by a factor of approximately three.

We determined the parameters β , b , and a for the filter function using the exact diagonalization method. Since the one-dimensional transverse-field Ising model can be solved efficiently, these parameters can readily be obtained even for larger system sizes. For situations where exact solutions are not available (e.g., mixed-field Ising models), quantum Monte Carlo or tensor-network methods may be used to estimate β , b , and a . In addition, for certain parameter regimes of the

Hubbard and Heisenberg models, values of E_0 may be found in the literature [4–13]. We emphasize, however, that precise estimates of these low-lying eigenenergies are not strictly required, as long as β , a , and b are chosen to (approximately) satisfy the condition on the filter function in Eq. (14). It is also worth noting that, in the NISQ era with limited quantum resources, the modification of the filter function arising from time discretization can have a more significant impact on the systematic error of the protocol than modest inaccuracies in estimating these parameters.

While we have fixed the form of the filter function and the time-discretization scheme as in Eq. (23), these choices may also be optimized to achieve fast convergence while minimizing quantum resources, such as the number of two-qubit gates. For instance, one may adopt a coarser time-discretization grid at early time steps m to reduce resource overhead, and then refine the grid at later time steps to more accurately reproduce the step-function-like behavior of $\tilde{f}(\omega)$. Such an optimization is conceptually analogous to optimized imaginary-time evolution in classical computing [9, 50] and represents a promising direction for future developments in dissipative ground-state preparation.

ACKNOWLEDGMENTS

We thank Anshuman Bhartdawaj, Haruki Emori, Masanao Ozawa, and Maho Nakata for valuable discussions. We also thank Clemens Gneiting for helpful comments. K. S. is supported by JSPS KAKENHI Grant No. JP22K03520. T. H. is supported by JSPS KAKENHI Grants No. JP24K00630 and No. JP25K01002. S. Y. is supported by JSPS KAKENHI Grant No. JP24K02948. This work is based in part on results obtained from a project (JPNP20017), subsidized by the New Energy and Industrial Technology Development Organization (NEDO), Japan. We also acknowledge funding from JST COI-NEXT (Grant No. JPMJPF2221). Furthermore, we acknowledge support from the UTokyo Quantum Initiative, the RIKEN TRIP initiative (RIKEN Quantum), and the COE research grant in computational science from Hyogo Prefecture and Kobe City through the Foundation for Computational Science.

Appendix A: Derivation of the Kraus representation

In this Appendix, we derive the Kraus representation of Γ_K given on the right-hand side of Eq. (7) and provide additional remarks on its structure.

1. Derivation of Eq. (7)

We begin by considering the Taylor expansion of the dilated unitary operator $\hat{W}(\sqrt{\tau})$ defined in Eq. (3):

$$\hat{W}(\sqrt{\tau}) = \sum_{k=0}^{\infty} c_k \hat{K}^k = \sum_{k=0}^{\infty} (c_{2k} \hat{K}^{2k} + c_{2k+1} \hat{K}^{2k+1}), \quad (\text{A1})$$

where $c_k = (-i\sqrt{\tau})^k/k!$. The decomposition into even and odd powers is made for clarity. From Eq. (4), we obtain

$$\hat{K}^{2k} = |0\rangle\langle 0|_a \otimes (\hat{K}^\dagger \hat{K})^k + |1\rangle\langle 1|_a \otimes (\hat{K} \hat{K}^\dagger)^k, \quad (\text{A2})$$

$$\hat{K}^{2k+1} = |1\rangle\langle 0|_a \otimes \hat{K} (\hat{K}^\dagger \hat{K})^k + |0\rangle\langle 1|_a \otimes (\hat{K}^\dagger \hat{K})^k \hat{K}^\dagger, \quad (\text{A3})$$

showing that \hat{K}^{2k} is diagonal and \hat{K}^{2k+1} is off-diagonal in the ancilla-qubit subspace. Thus, the matrix representation of $\hat{W}(\sqrt{\tau})$ reads

$$\begin{aligned} \hat{W}(\sqrt{\tau}) &= \begin{bmatrix} \sum_{k=0}^{\infty} c_{2k} (\hat{K}^\dagger \hat{K})^k & \sum_{k=0}^{\infty} c_{2k+1} (\hat{K}^\dagger \hat{K})^k \hat{K}^\dagger \\ \hat{K} \sum_{k=0}^{\infty} c_{2k+1} (\hat{K}^\dagger \hat{K})^k & \sum_{k=0}^{\infty} c_{2k} (\hat{K} \hat{K}^\dagger)^k \end{bmatrix} \\ &= \begin{bmatrix} \hat{C} & -i\sqrt{\tau} \hat{S}_c \hat{K}^\dagger \\ -i\sqrt{\tau} \hat{K} \hat{S}_c & \hat{C}' \end{bmatrix} \\ &= \begin{bmatrix} \hat{M}_0 & -\hat{M}_1^\dagger \\ \hat{M}_1 & \hat{C}' \end{bmatrix}, \end{aligned} \quad (\text{A4})$$

where the cosine and cardinal-sine expansions defined in Eqs. (8) and (9) have been used, and $\hat{C}' = \cos \sqrt{\tau} \hat{K} \hat{K}^\dagger$. In the final expression, we identify the Kraus operators $\hat{M}_0 = \langle 0 | \hat{W}(\sqrt{\tau}) | 0 \rangle_a = \hat{C}$ and $\hat{M}_1 = \langle 1 | \hat{W}(\sqrt{\tau}) | 0 \rangle_a = -i\sqrt{\tau} \hat{K} \hat{S}_c$.

Using the block-matrix form of $\hat{W}(\sqrt{\tau})$, Eq. (6) can be written as

$$\begin{aligned} \hat{\sigma}(\tau) &= \hat{W}(\sqrt{\tau}) (|0\rangle\langle 0|_a \otimes \hat{\rho}) \hat{W}^\dagger(\sqrt{\tau}) \\ &= \begin{bmatrix} \hat{M}_0 & -\hat{M}_1^\dagger \\ \hat{M}_1 & \hat{C}' \end{bmatrix} \begin{bmatrix} \hat{\rho} & 0 \\ 0 & 0 \end{bmatrix} \begin{bmatrix} \hat{M}_0^\dagger & \hat{M}_1^\dagger \\ -\hat{M}_1 & \hat{C}'^\dagger \end{bmatrix} \\ &= \begin{bmatrix} \hat{M}_0 \hat{\rho} \hat{M}_0^\dagger & \hat{M}_0 \hat{\rho} \hat{M}_1^\dagger \\ \hat{M}_1 \hat{\rho} \hat{M}_0^\dagger & \hat{M}_1 \hat{\rho} \hat{M}_1^\dagger \end{bmatrix}. \end{aligned} \quad (\text{A5})$$

Tracing out the ancilla then yields Eq. (7): $\Gamma_K[\hat{\rho}] = \text{Tr}_a[\hat{\sigma}(\tau)] = \hat{M}_0 \hat{\rho} \hat{M}_0^\dagger + \hat{M}_1 \hat{\rho} \hat{M}_1^\dagger$, which is the Kraus representation of the map.

2. Lindblad dynamics

As a remark on Γ_K , we note that its lowest-order expansion coincides with a Lindblad dynamics with the jump operator \hat{K} . By explicitly extracting the terms proportional to τ^0 and τ^1 from Eq. (7), we obtain

$$\Gamma_K[\hat{\rho}] = \hat{\rho} + \tau \hat{K} \hat{\rho} \hat{K}^\dagger - \frac{\tau}{2} \{ \hat{K}^\dagger \hat{K}, \hat{\rho} \} + O(\tau^2). \quad (\text{A6})$$

Therefore, in the small τ limit, Γ_K reduces to the Lindblad evolution generated by the jump operator \hat{K} , as discussed in Ref. [42].

Appendix B: Fourier transform of the filter function

In this Appendix, we derive the Fourier transform $f(s)$ of the filter function $\tilde{f}(\omega)$, following the definitions in Eqs. (16) and (29). This derivation leads directly to the expression given in Eq. (30).

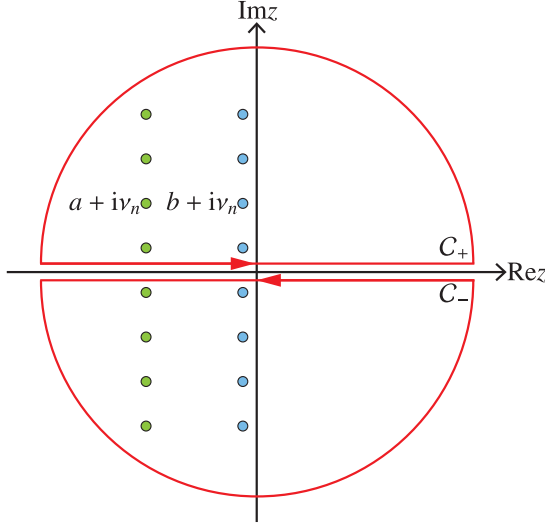


FIG. 6. Schematic illustration of the contours C_+ and C_- in the complex z -plane used to evaluate the Fourier transform $f(s)$ of the filter function. The green and blue dots denote the shifted fermionic Matsubara frequencies $a + iv_n$ and $b + iv_n$, respectively.

First, at $s = 0$, we obtain

$$f(0) = \int_{-\infty}^{\infty} \frac{d\omega}{2\pi} [n_F(\beta(\omega - b)) - n_F(\beta(\omega - a))] = \frac{b - a}{2\pi}, \quad (B1)$$

which is independent of β . In deriving Eq. (B1), we have used the identity $n_F(\beta(\omega - b)) = \partial_\omega \left[-\frac{1}{\beta} \ln(1 + e^{-\beta(\omega-b)}) \right]$.

Next, to evaluate $f(s)$ for $s \neq 0$, we employ contour integration in the complex z -plane and use the fact that $n_F(\beta(z-a))$ has poles at

$$z = a + iv_n, \quad iv_n = i \frac{(2n+1)\pi}{\beta}, \quad (B2)$$

each with residue $-\beta$, where v_n are the fermionic Matsubara frequencies and n is an integer [51]. Depending on the sign of s , we rewrite $f(s)$ as a contour integral:

$$f(s) = \begin{cases} \frac{1}{2\pi} \oint_{C_+} dz \tilde{f}(z) e^{-izs} & (s < 0) \\ -\frac{1}{2\pi} \oint_{C_-} dz \tilde{f}(z) e^{-izs} & (s > 0) \end{cases} \quad (B3)$$

where the contour C_+ (C_-) consists of the real axis together with an infinite semicircular arc enclosing the upper (lower) half of the complex z -plane in the counterclockwise direction (see Fig. 6). The radius of the semicircle is taken to infinity at the end of the calculation. The choice of contour is dictated by the factor e^{-izs} : for $s < 0$ ($s > 0$), the contribution from the arc at infinity vanishes only when the contour is closed in the upper (lower) half-plane. Since C_+ (C_-) encloses the poles at $a + iv_n$ and $b + iv_n$ in the upper (lower) half-plane, the residue

theorem gives

$$f(s) = \begin{cases} -\frac{i}{\beta} (e^{-ibs} - e^{-ias}) \sum_{n=0}^{\infty} e^{\frac{(2n+1)\pi}{\beta}s} & (s < 0), \\ \frac{i}{\beta} (e^{-ibs} - e^{-ias}) \sum_{n=0}^{\infty} e^{-\frac{(2n+1)\pi}{\beta}s} & (s > 0). \end{cases} \quad (B4)$$

To unify these expressions, we use the geometric-series representation of the hyperbolic cosecant,

$$\frac{1}{\sinh s} = \frac{2}{e^s - e^{-s}} \begin{cases} -2 \sum_{n=0}^{\infty} e^{(2n+1)s} & (s < 0), \\ 2 \sum_{n=0}^{\infty} e^{-(2n+1)s} & (s > 0), \end{cases} \quad (B5)$$

which allows Eq. (B4) to be written compactly as

$$f(s) = \frac{i(e^{-ibs} - e^{-ias})}{2\beta \sinh \frac{\pi}{\beta}s} = e^{-i\frac{b+a}{2}s} \frac{\sin \frac{b-a}{2}s}{\beta \sinh \frac{\pi}{\beta}s}. \quad (B6)$$

Finally, we readily verify that $\lim_{s \rightarrow 0} f(s) = (b-a)/2\pi$, which exactly matches the value of $f(0)$ obtained in Eq. (B1), confirming that $f(s)$ is continuous at $s = 0$. Thus we obtain Eq. (30).

Appendix C: Time discretization of the OFT

We analyze the errors arising from the regularization of the OFT in Eq. (15), which include the time-discretization (aliasing) error, ϵ_{alias} , and the truncation (leakage) error, ϵ_{leak} .

1. Time discretization

We begin by analyzing the time-discretization error, i.e., the aliasing error. To this end, we employ Poisson's resummation formula,

$$\begin{aligned} & \Delta_s \sum_{l=-\infty}^{\infty} f(l\Delta_s) \hat{A}(l\Delta_s) \\ &= \int_{-\infty}^{\infty} dt f(t) \hat{A}(t) + \sum_{k \in \mathbb{Z} \setminus \{0\}} \int_{-\infty}^{\infty} dt e^{-i2\pi kt/\Delta_s} f(t) \hat{A}(t), \end{aligned} \quad (C1)$$

which leads to the aliasing error

$$\begin{aligned} \epsilon_{\text{alias}} &= \left\| \int_{-\infty}^{\infty} dt f(t) \hat{A}(t) - \Delta_s \sum_{l=-\infty}^{\infty} f(l\Delta_s) \hat{A}(l\Delta_s) \right\| \\ &= \left\| \sum_{k \in \mathbb{Z} \setminus \{0\}} \int_{-\infty}^{\infty} dt e^{-i2\pi kt/\Delta_s} f(t) \hat{A}(t) \right\| \\ &= \left\| \sum_{\nu \in B_H} \sum_{k \in \mathbb{Z} \setminus \{0\}} \int_{-\infty}^{\infty} dt e^{-i2\pi kt/\Delta_s} f(t) e^{i\nu t} \hat{A}_\nu \right\| \\ &= \left\| \sum_{\nu \in B_H} \sum_{k \in \mathbb{Z} \setminus \{0\}} \tilde{f}(\nu - 2\pi k/\Delta_s) \hat{A}_\nu \right\|. \end{aligned} \quad (C2)$$

Here, $\|\cdot\|$ denotes the spectral norm, B_H is the set of all eigenvalue differences of \hat{H} , and $\hat{A}_v \equiv \sum_{i,j: E_i - E_j = v} |E_i\rangle\langle E_i| \hat{A} |E_j\rangle\langle E_j|$. For the filter function defined in Eq. (29), we obtain the bound

$$\epsilon_{\text{alias}} \leq 4^N \|\hat{A}\| \sum_{k \in \mathbb{Z} \setminus \{0\}} \tilde{f}(2\|\hat{H}\| - 2\pi k/\Delta_s). \quad (\text{C3})$$

The sum evaluates to

$$\begin{aligned} & \sum_{k \in \mathbb{Z} \setminus \{0\}} \tilde{f}(2\|\hat{H}\| - 2\pi k/\Delta_s) \\ &= \sum_{k \in \mathbb{Z} \setminus \{0\}} \frac{1}{e^{-\beta(2\pi k/\Delta_s - 2\|\hat{H}\| + b)} + 1} - \frac{1}{e^{-\beta(2\pi k/\Delta_s - 2\|\hat{H}\| + a)} + 1} \\ &\leq e^{2\beta\|\hat{H}\|} (e^{-\beta a} - e^{-\beta b}) \sum_{k > 0} e^{-2\pi\beta k/\Delta_s} \\ &\quad + e^{-2\beta\|\hat{H}\|} (e^{\beta a} - e^{\beta b}) \sum_{k < 0} e^{2\pi\beta k/\Delta_s} \\ &\leq e^{2\beta\|\hat{H}\|} (e^{-\beta a} - e^{-\beta b}) \frac{e^{-2\pi\beta/\Delta_s}}{1 - e^{-2\pi\beta/\Delta_s}}. \end{aligned} \quad (\text{C4})$$

Therefore, the aliasing error is bounded as

$$\epsilon_{\text{alias}} \leq \frac{\|\hat{A}\| (e^{-\beta a} - e^{-\beta b})}{1 - e^{-2\pi\beta/\Delta_s}} 4^N e^{-2\beta(\pi/\Delta_s - \|\hat{H}\|)}. \quad (\text{C5})$$

2. Truncation of the infinite sum

We now analyze the error arising from truncating the infinite sum, i.e., the leakage error:

$$\begin{aligned} \epsilon_{\text{leak}} &= \left\| \sum_{|l| > M_s} f(l\Delta_s) \right\| \leq \frac{4}{\beta(1 - e^{-\frac{2\pi\Delta_s}{\beta} M_s})} \sum_{l=M_s}^{\infty} e^{-\frac{\pi\Delta_s}{\beta} l} \\ &= \frac{4}{\beta(1 - e^{-\frac{2\pi}{\beta} S_s})(1 - e^{-\frac{\pi\Delta_s}{\beta}})} e^{-\frac{\pi\Delta_s}{\beta} S_s}, \end{aligned} \quad (\text{C6})$$

where in the first inequality we used the bound $|f(s)| \leq 2\beta^{-1} e^{-\frac{\pi}{\beta} s} (1 - e^{-\frac{2\pi}{\beta} S_s})^{-1}$ for $s \geq S_s$.

Appendix D: τ dependence of the convergence

In this Appendix, we examine how the convergence behavior depends on the parameter τ using noiseless simulations. We recall that $\sqrt{\tau}$ plays the role of an ‘‘interaction time’’ between the system and the ancilla, as seen in Eq. (25). Figure 7(a) shows the noiseless simulation results for the energy expectation value of the $N = 6$ system for $\tau = 0.1, 0.5, 1, 4, 8$, and 12, with the model parameters fixed to $J = -1$ and $B_X = -1.2$. We observe that the convergence rate with respect to the time step m depends strongly on τ . For small τ (e.g., $\tau = 0.1$), the energy decreases only slowly as a function of m , whereas the convergence becomes progressively faster as τ increases. The most rapid decrease is obtained at $\tau = 4$, and essentially the same behavior is seen at $\tau = 8$. However, further increasing τ to $\tau = 12$ results in slower convergence compared with the optimal region around $\tau = 4$ -8.

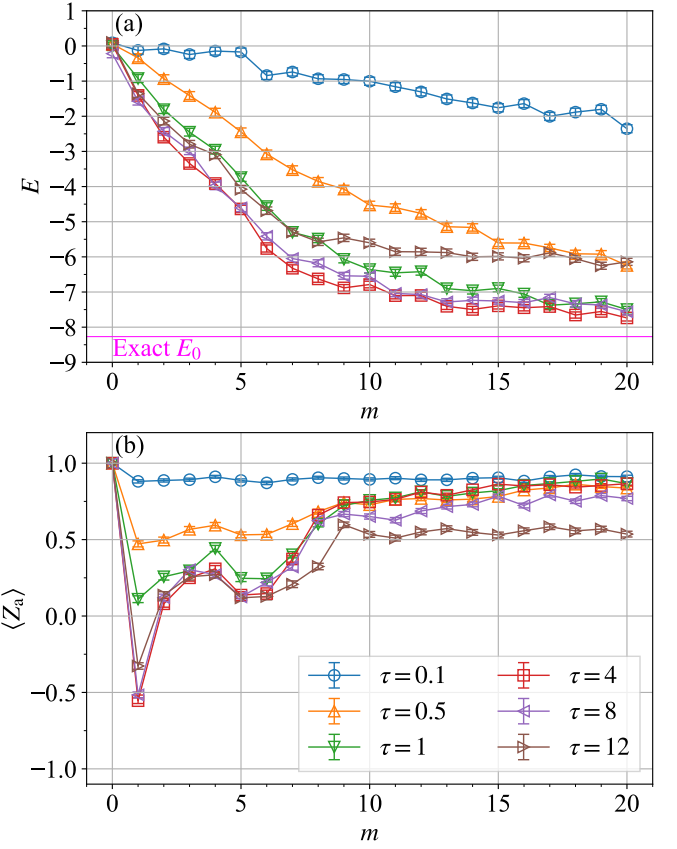


FIG. 7. Noiseless simulation results for (a) the energy $E(m)$ and (b) the expectation value of the ancilla Pauli-Z operator as functions of the time steps m for the $N = 6$ transverse-field Ising model at various values of the dissipation time step τ . The model parameters are $J = -1$ and $B_X = -1.2$.

To gain further insight into the τ -dependence of the convergence, we examine the probabilities of measuring the ancilla qubit in the states $|0\rangle_a$ and $|1\rangle_a$. Equation (A5) implies that Γ_K can be written as

$$\Gamma_K[\hat{\rho}] = \text{Tr}_a [|0\rangle\langle 0|_a \otimes \hat{M}_0 \hat{\rho} \hat{M}_0^\dagger + |1\rangle\langle 1|_a \otimes \hat{M}_1 \hat{\rho} \hat{M}_1^\dagger], \quad (\text{D1})$$

where the off-diagonal terms in the ancilla subspace have been omitted, as they vanish upon tracing out the ancilla. The probabilities of obtaining outcomes 0 and 1 when measuring the ancilla qubit are therefore given by

$$p_0 = \text{Tr}[\hat{M}_0 \hat{\rho} \hat{M}_0^\dagger], \quad (\text{D2})$$

$$p_1 = \text{Tr}[\hat{M}_1 \hat{\rho} \hat{M}_1^\dagger], \quad (\text{D3})$$

respectively. The completeness relation in Eq. (11) ensures that $p_0 + p_1 = 1$ for any normalized state satisfying $\text{Tr}[\hat{\rho}] = 1$.

Figure 7(b) shows the noiseless simulation results for the expectation value $\langle \hat{Z}_a \rangle = p_0 - p_1 = 2p_0 - 1$ of the ancilla qubit at time step m . Here, $\langle \hat{Z}_a \rangle$ is estimated from the measurement outcome of the ancilla qubit just before reset (classically controlled Pauli-X) operation at time step m . By definition, $\langle \hat{Z}_a \rangle = 1$ at $m = 0$, since the ancilla is initialized in the state

$|0\rangle_a$. Note also that, once the system has converged to the ground state, the ancilla will be measured in $|0\rangle_a$. At small τ (e.g., $\tau = 0.1$), $\langle \hat{Z}_a \rangle$ remains close to 1, indicating that the ancilla is almost always measured in the state $|0\rangle_a$. As τ increases, $\langle \hat{Z}_a \rangle$ decreases, reflecting an increased likelihood of obtaining the outcome $|1\rangle_a$. In particular, the value of $\langle \hat{Z}_a \rangle$ at the first time step $m = 1$ exhibits the strongest dependence on τ . Assuming that τ is small, the Kraus operators may be approximated as $\hat{M}_0 \approx 1 - \frac{1}{2}\tau\hat{K}^\dagger\hat{K}$ and $\hat{M}_1 \approx -i\sqrt{\tau}\hat{K}$, using Eqs. (8) and (9). Accordingly, the ancilla outcome probabilities are approximated up to $O(\tau)$ as

$$p_0 = \text{Tr}[\hat{M}_0\hat{\rho}\hat{M}_0^\dagger] \approx 1 - \tau\text{Tr}[\hat{K}\hat{\rho}\hat{K}^\dagger], \quad (\text{D4})$$

$$p_1 = \text{Tr}[\hat{M}_1\hat{\rho}\hat{M}_1^\dagger] \approx \tau\text{Tr}[\hat{K}\hat{\rho}\hat{K}^\dagger]. \quad (\text{D5})$$

These expressions are consistent with the numerical observation that p_0 decreases with increasing τ in the small- τ regime. The post-measurement states $\hat{\rho}_0$ and $\hat{\rho}_1$ of the system corresponding to ancilla outcomes $|0\rangle\langle 0|_a$ and $|1\rangle\langle 1|_a$ are given by

$$p_0\hat{\rho}_0 = \hat{M}_0\hat{\rho}\hat{M}_0^\dagger \approx \hat{\rho} - \frac{\tau}{2}\{\hat{K}^\dagger\hat{K}, \hat{\rho}\}, \quad (\text{D6})$$

$$p_1\hat{\rho}_1 = \hat{M}_1\hat{\rho}\hat{M}_1^\dagger \approx \tau\hat{K}\hat{\rho}\hat{K}^\dagger, \quad (\text{D7})$$

which give the explicit dependence on τ to leading order. Al-

though heuristic, the noiseless simulations suggest that increasing τ does increase p_1 , i.e., the population of the branch associated with $\hat{\rho}_1$. However, a larger p_1 does not necessarily imply faster convergence of the overall dissipative dynamics. For general τ , the Kraus operators involve trigonometric functions of $\sqrt{\tau}\hat{K}^\dagger\hat{K}$, and thus both the energy $E(m)$ and the ancilla expectation value $\langle \hat{Z}_a \rangle$ can exhibit nonmonotonic dependence on τ . Indeed, such nonmonotonic behavior is observed numerically when τ is increased up to $\tau = 12$. This indicates the presence of an optimal τ that yields the fastest convergence to the steady state when the other parameters are fixed.

Appendix E: Zero-noise extrapolation

In this Appendix, we present the details of the ZNE procedure for the $N = 6$ and $N = 19$ systems. Figure 8 shows the linear and exponential fits applied to the energy expectation values obtained from the hardware experiments for the $N = 6$ system as functions of the noise-scaling factor G at time steps $m = 5, 10, 15$, and 20 . Similarly, Fig. 9 displays the linear and exponential fits for the $N = 19$ system at $m = 10, 20$, and 30 .

[1] D. Wu, R. Rossi, F. Vicentini, N. Astrakhantsev, F. Becca, X. Cao, J. Carrasquilla, F. Ferrari, A. Georges, M. Hibat-Allah, M. Imada, A. M. Läuchli, G. Mazzola, A. Mezzacapo, A. Millis, J. Robledo Moreno, T. Neupert, Y. Nomura, J. Nys, O. Parcollet, R. Pohle, I. Romero, M. Schmid, J. M. Silvester, S. Sorella, L. F. Tocchio, L. Wang, S. R. White, A. Wittek, Q. Yang, Y. Yang, S. Zhang, and G. Carleo, Variational benchmarks for quantum many-body problems, *Science* **366**, 296–301 (2024).

[2] J. E. Hirsch, Two-dimensional hubbard model: Numerical simulation study, *Phys. Rev. B* **31**, 4403 (1985).

[3] D. Tahara and M. Imada, Variational monte carlo method combined with quantum-number projection and multi-variable optimization, *Journal of the Physical Society of Japan* **77**, 114701 (2008).

[4] J. P. F. LeBlanc, A. E. Antipov, F. Becca, I. W. Bulik, G. K.-L. Chan, C.-M. Chung, Y. Deng, M. Ferrero, T. M. Henderson, C. A. Jiménez-Hoyos, E. Kozik, X.-W. Liu, A. J. Millis, N. V. Prokof'ev, M. Qin, G. E. Scuseria, H. Shi, B. V. Svistunov, L. F. Tocchio, I. S. Tupitsyn, S. R. White, S. Zhang, B.-X. Zheng, Z. Zhu, and E. Gull (Simons Collaboration on the Many-Electron Problem), Solutions of the two-dimensional hubbard model: Benchmarks and results from a wide range of numerical algorithms, *Phys. Rev. X* **5**, 041041 (2015).

[5] B.-X. Zheng, C.-M. Chung, P. Corboz, G. Ehlers, M.-P. Qin, R. M. Noack, H. Shi, S. R. White, S. Zhang, and G. K.-L. Chan, Stripe order in the underdoped region of the two-dimensional hubbard model, *Science* **358**, 1155–1160 (2017).

[6] Y. Nomura, A. S. Darmawan, Y. Yamaji, and M. Imada, Restricted boltzmann machine learning for solving strongly correlated quantum systems, *Phys. Rev. B* **96**, 205152 (2017).

[7] K. Ido, T. Ohgoe, and M. Imada, Competition among various charge-inhomogeneous states and d -wave superconducting state in hubbard models on square lattices, *Phys. Rev. B* **97**, 045138 (2018).

[8] K. Seki and S. Sorella, Benchmark study of an auxiliary-field quantum monte carlo technique for the hubbard model with shifted-discrete hubbard-stratonovich transformations, *Phys. Rev. B* **99**, 144407 (2019).

[9] S. Sorella, Systematically improvable mean-field variational ansatz for strongly correlated systems: Application to the hubbard model, *Phys. Rev. B* **107**, 115133 (2023).

[10] A. W. Sandvik, Finite-size scaling of the ground-state parameters of the two-dimensional heisenberg model, *Phys. Rev. B* **56**, 11678 (1997).

[11] Y. Iqbal, F. Becca, S. Sorella, and D. Poilblanc, Gapless spin-liquid phase in the kagome spin- $\frac{1}{2}$ heisenberg antiferromagnet, *Phys. Rev. B* **87**, 060405 (2013).

[12] Y. Iqbal, W.-J. Hu, R. Thomale, D. Poilblanc, and F. Becca, Spin liquid nature in the heisenberg $J_1 - J_2$ triangular antiferromagnet, *Phys. Rev. B* **93**, 144411 (2016).

[13] Y. Nomura and M. Imada, Dirac-type nodal spin liquid revealed by refined quantum many-body solver using neural-network wave function, correlation ratio, and level spectroscopy, *Phys. Rev. X* **11**, 031034 (2021).

[14] N. Yoshioka, T. Okubo, Y. Suzuki, Y. Koizumi, and W. Mizukami, Hunting for quantum-classical crossover in condensed matter problems, *npj Quantum Information* **10**, 10.1038/s41534-024-00839-4 (2024).

[15] O. Lanes, M. Beiji, A. D. Corcoles, C. Dalyac, J. M. Gambetta, L. Henriet, A. Javadi-Abhari, A. Kandala, A. Mezzacapo, C. Porter, S. Sheldon, J. Watrous, C. Zoufal, A. Dauphin, and B. Peropadre, *A framework for quantum advantage* (2025),

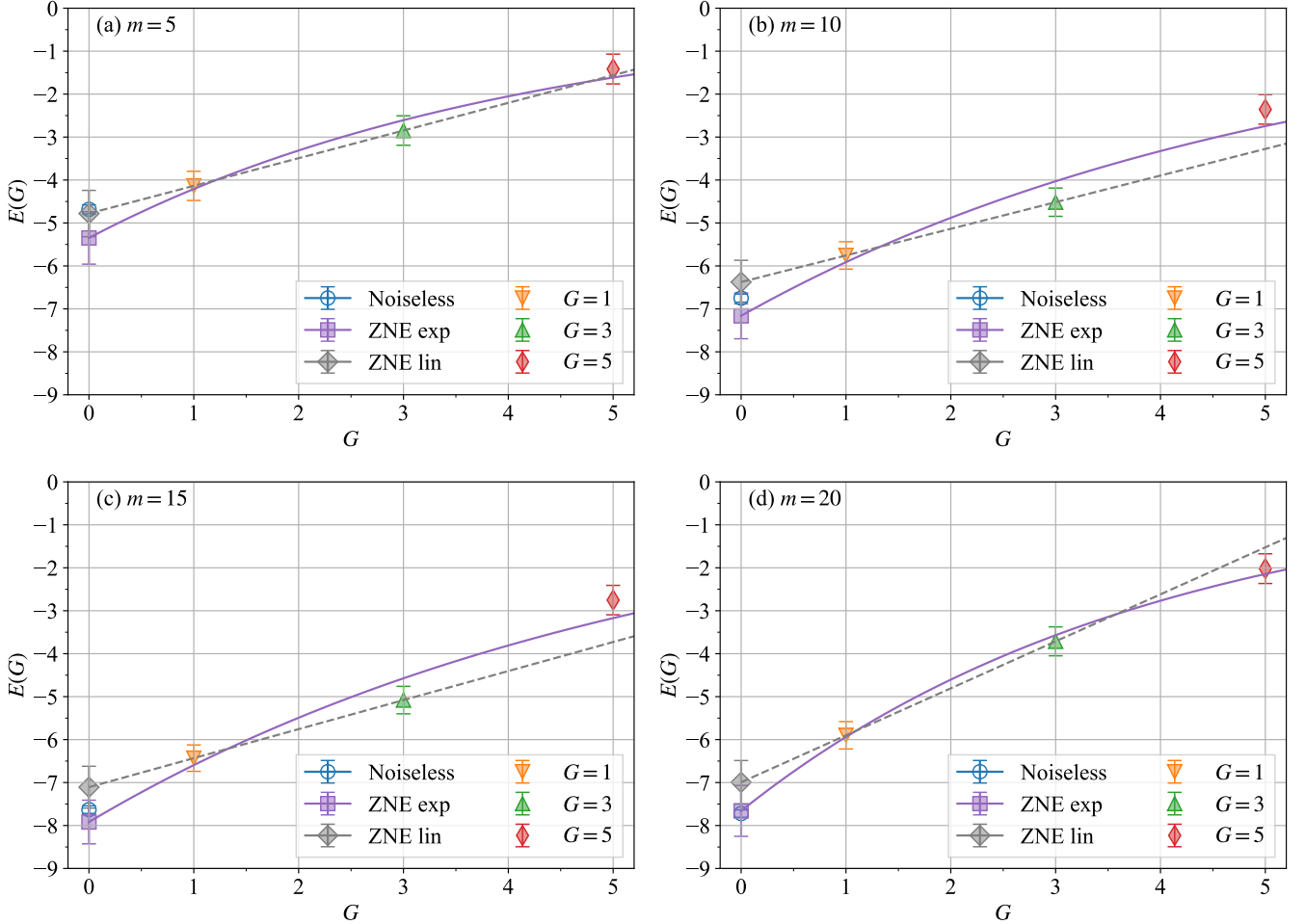


FIG. 8. Energy as a function of the noise-scaling factor G at time steps (a) $m = 5$, (b) $m = 10$, (c) $m = 15$, and (d) $m = 20$ for the $N = 6$ transverse-field Ising model with parameters $J = -1$ and $B_X = -1.2$. Solid curves and dashed lines indicate the exponential fits, $\tilde{a} \exp(\tilde{b}G)$, and the linear fits, $\tilde{a}G + \tilde{b}$, respectively, applied to the experimental data. The data at $G = 1, 3$, and 5 are used for the exponential fits, whereas only the data at $G = 1$ and 3 are used for the linear fits. Error bars at $G = 1, 3$, and 5 indicate the standard deviations of the measurements, while those at $G = 0$ (the extrapolated values) include the uncertainties arising from the extrapolation. Noiseless simulation results are also shown as blue circles at $G = 0$. Each data point at $G = 1, 3$, and 5 is obtained using 100 measurement shots, whereas the noiseless results are obtained using 1000 measurement shots.

arXiv:2506.20658 [quant-ph].

[16] A. Peruzzo, J. McClean, P. Shadbolt, M.-H. Yung, X.-Q. Zhou, P. J. Love, A. Aspuru-Guzik, and J. L. O'Brien, A variational eigenvalue solver on a photonic quantum processor, *Nature Communications* **5**, 10.1038/ncomms5213 (2014).

[17] A. Kandala, A. Mezzacapo, K. Temme, M. Takita, M. Brink, J. M. Chow, and J. M. Gambetta, Hardware-efficient variational quantum eigensolver for small molecules and quantum magnets, *Nature* **549**, 242–246 (2017).

[18] J. R. McClean, S. Boixo, V. N. Smelyanskiy, R. Babbush, and H. Neven, Barren plateaus in quantum neural network training landscapes, *Nature Communications* **9**, 10.1038/s41467-018-07090-4 (2018).

[19] K. Kanno, M. Kohda, R. Imai, S. Koh, K. Mitarai, W. Mizukami, and Y. O. Nakagawa, Quantum-Selected Configuration Interaction: classical diagonalization of Hamiltonians in subspaces selected by quantum computers, *arXiv e-prints*, arXiv:2302.11320 (2023), arXiv:2302.11320 [quant-ph].

[20] J. Robledo-Moreno, M. Motta, H. Haas, A. Javadi-Abhari, P. Jurcevic, W. Kirby, S. Martiel, K. Sharma, S. Sharma, T. Shirakawa, I. Sitzdikov, R.-Y. Sun, K. J. Sung, M. Takita, M. C. Tran, S. Yunoki, and A. Mezzacapo, Chemistry beyond the scale of exact diagonalization on a quantum-centric supercomputer, *Science Advances* **11**, 10.1126/sciadv.adu9991 (2025).

[21] Y. O. Nakagawa, M. Kamoshita, W. Mizukami, S. Sudo, and Y.-y. Ohnishi, Adapt-qsci: Adaptive construction of an input state for quantum-selected configuration interaction, *Journal of Chemical Theory and Computation* **20**, 10817–10825 (2024).

[22] K. Sugisaki, S. Kanno, T. Itoko, R. Sakuma, and N. Yamamoto, Hamiltonian simulation-based quantum-selected configuration interaction for large-scale electronic structure calculations with a quantum computer, *Physical Chemistry Chemical Physics* **27**, 20869–20884 (2025).

[23] M. Mikkelsen and Y. O. Nakagawa, Quantum-selected configuration interaction with time-evolved state, *Phys. Rev. Res.* **7**, 043043 (2025).

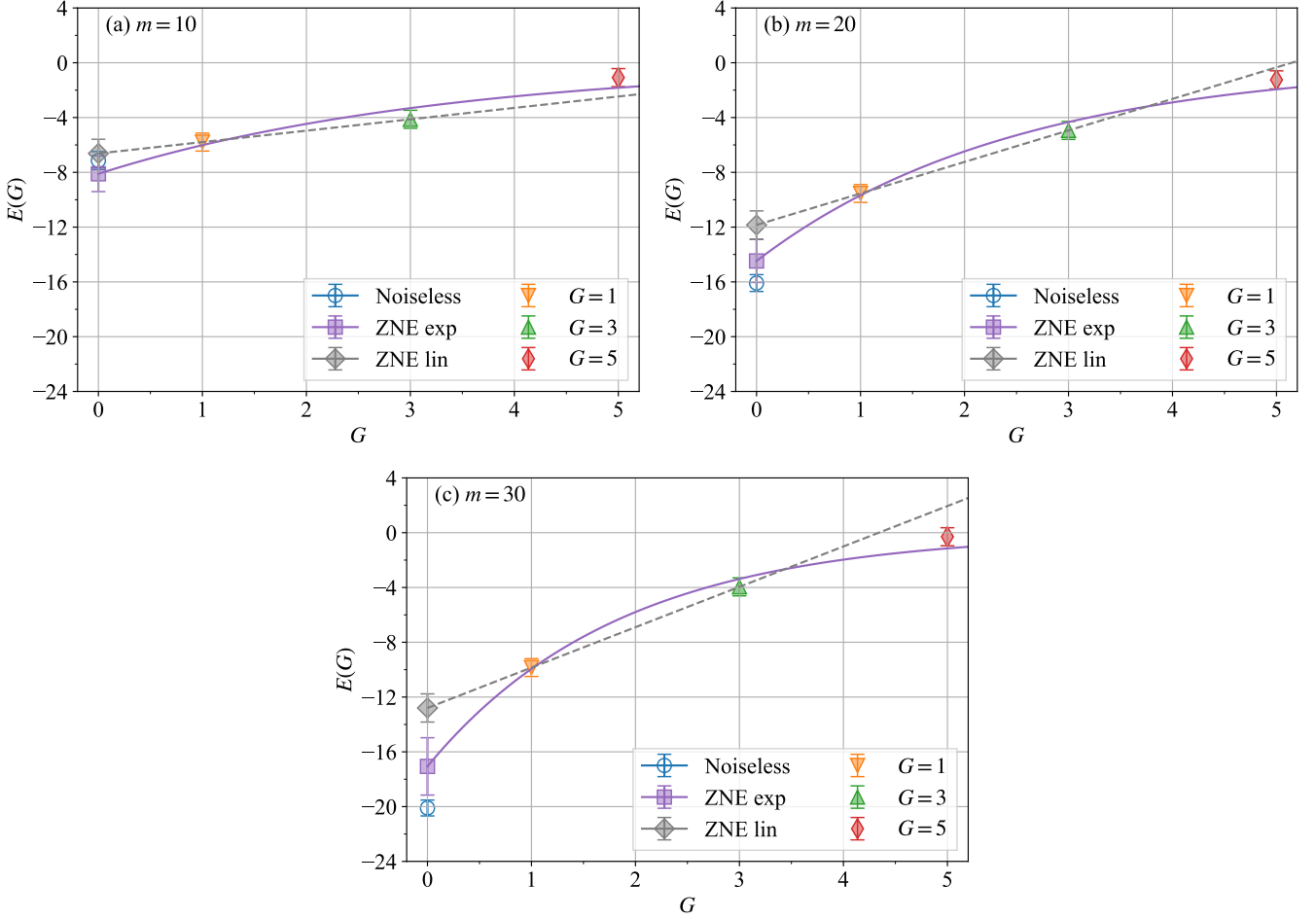


FIG. 9. Same as Fig. 8, but for the $N = 19$ transverse-field Ising model at time steps (a) $m = 10$, (b) $m = 20$, and (c) $m = 30$.

[24] J. Yu, J. Robledo Moreno, J. T. Iosue, L. Bertels, D. Claudino, B. Fuller, P. Groszkowski, T. S. Humble, P. Jurcevic, W. Kirby, T. A. Maier, M. Motta, B. Pokharel, A. Seif, A. Shehata, K. J. Sung, M. C. Tran, V. Tripathi, A. Mezzacapo, and K. Sharma, Quantum-Centric Algorithm for Sample-Based Krylov Diagonalization, [arXiv e-prints](https://arxiv.org/abs/2501.09702), [arXiv:2501.09702 \[quant-ph\]](https://arxiv.org/abs/2501.09702).

[25] Y. Alexeev, M. Amsler, P. Baity, M. A. Barroca, S. Bassini, T. Battelle, D. Camps, D. Casanova, Y. J. Choi, F. T. Chong, C. Chung, C. Codella, A. D. Corcoles, J. Cruise, A. Di Meglio, J. Dubois, I. Duran, T. Eckl, S. Economou, S. Eidenbenz, B. Elmegreen, C. Fare, I. Faro, C. Sanz Fernández, R. Neumann Barros Ferreira, K. Fuji, B. Fuller, L. Gagliardi, G. Galli, J. R. Glick, I. Gobbi, P. Gokhale, S. de la Puente Gonzalez, J. Greiner, B. Gropp, M. Grossi, E. Gull, B. Healy, B. Huang, T. S. Humble, N. Ito, A. F. Izmaylov, A. Javadi-Abhari, D. Jennewein, S. Jha, L. Jiang, B. Jones, W. A. de Jong, P. Jurcevic, W. Kirby, S. Kister, M. Kitagawa, J. Klassen, K. Klymko, K. Koh, M. Kondo, D. Murat Kurkcuoglu, K. Kurowski, T. Laino, R. Landfield, M. Leininger, V. Leyton-Ortega, A. Li, M. Lin, J. Liu, N. Lorente, A. Luckow, S. Martiel, F. Martin-Fernandez, M. Martonosi, C. Marvinney, A. Castaneda Medina, D. Merten, A. Mezzacapo, K. Michielsen, A. Mitra, T. Mittal, K. Moon, J. Moore, M. Motta, Y.-H. Na, Y. Nam, P. Narang, Y.-y. Ohnishi, D. Ottaviani, M. Otten, S. Pakin, V. R. Pascuzzi, E. Penault, T. Piontek, J. Pitera, P. Rall, G. Subramanian Ravi, N. Robertson, M. Rossi, P. Rydlichowski, H. Ryu, G. Samsonidze, M. Sato, N. Saurabh, V. Sharma, K. Sharma, S. Shin, G. Slessman, M. Steiner, I. Sitzikov, I.-S. Suh, E. Switzer, W. Tang, J. Thompson, S. Todo, M. Tran, D. Trenev, C. Trott, H.-H. Tseng, E. Tureci, D. García Valinas, S. Vallecorsa, C. Wever, K. Wojciechowski, X. Wu, S. Yoo, N. Yoshioka, V. Wen-zhe Yu, S. Yunoki, S. Zhuk, and D. Zubarev, Quantum-centric Supercomputing for Materials Science: A Perspective on Challenges and Future Directions, *Future Generation Computer Systems* **160**, 666 (2024).

[26] S. Barison, J. Robledo Moreno, and M. Motta, Quantum-centric computation of molecular excited states with extended sample-based quantum diagonalization, *Quantum Science and Technology* **10**, 025034 (2025).

[27] T. Shirakawa, J. Robledo-Moreno, T. Itoko, V. Tripathi, K. Ueda, Y. Kawashima, L. Broers, W. Kirby, H. Pathak, H. Paik, M. Tsuji, Y. Kodama, M. Sato, C. Evangelinos, S. Seelam, R. Walkup, S. Yunoki, M. Motta, P. Jurcevic, H. Horii, and A. Mezzacapo, *Closed-loop calculations of electronic structure on a quantum processor and a classical supercomputer at full scale* (2025), [arXiv:2511.00224 \[quant-ph\]](https://arxiv.org/abs/2511.00224).

[28] A. A. Holmes, N. M. Tubman, and C. J. Umrigar, Heat-bath configuration interaction: An efficient selected configuration interaction algorithm inspired by heat-bath sampling, *Journal of*

[Chemical Theory and Computation](#) **12**, 3674–3680 (2016).

[29] P. Reinholdt, K. M. Ziems, E. R. Kjellgren, S. Coriani, S. P. A. Sauer, and J. Kongsted, Critical limitations in quantum-selected configuration interaction methods, [Journal of Chemical Theory and Computation](#) **21**, 6811–6822 (2025).

[30] J. M. Koh, S.-N. Sun, M. Motta, and A. J. Minnich, Measurement-induced entanglement phase transition on a superconducting quantum processor with mid-circuit readout, [Nature Physics](#) **19**, 1314–1319 (2023).

[31] E. Chertkov, Z. Cheng, A. C. Potter, S. Gopalakrishnan, T. M. Gatterman, J. A. Gerber, K. Gilmore, D. Gresh, A. Hall, A. Hankin, M. Matheny, T. Mengle, D. Hayes, B. Neyenhuis, R. Stutz, and M. Foss-Feig, Characterizing a non-equilibrium phase transition on a quantum computer, [Nature Physics](#) **19**, 1799–1804 (2023).

[32] M. Foss-Feig, D. Hayes, J. M. Dreiling, C. Figgatt, J. P. Gaebler, S. A. Moses, J. M. Pino, and A. C. Potter, Holographic quantum algorithms for simulating correlated spin systems, [Phys. Rev. Res.](#) **3**, 033002 (2021).

[33] M. DeCross, E. Chertkov, M. Kohagen, and M. Foss-Feig, Qubit-Reuse Compilation with Mid-Circuit Measurement and Reset, [Physical Review X](#) **13**, 041057 (2023).

[34] O. Shtanko and R. Movassagh, [Preparing thermal states on noiseless and noisy programmable quantum processors](#) (2023), [arXiv:2112.14688 \[quant-ph\]](#).

[35] C.-F. Chen, M. J. Kastoryano, F. G. S. L. Brandão, and A. Gilyén, Quantum Thermal State Preparation, [arXiv e-prints](#) (2023), [arXiv:2303.18224 \[quant-ph\]](#).

[36] C.-F. Chen, M. J. Kastoryano, and A. Gilyén, An efficient and exact noncommutative quantum Gibbs sampler, [arXiv e-prints](#) (2023), [arXiv:2311.09207 \[quant-ph\]](#).

[37] E. Brunner, L. Coopmans, G. Matos, M. Rosenkranz, F. Sauvage, and Y. Kikuchi, Lindblad engineering for quantum gibbs state preparation under the eigenstate thermalization hypothesis, [Quantum](#) **9**, 1843 (2025).

[38] J. Lloyd and D. A. Abanin, [Quantum thermal state preparation for near-term quantum processors](#) (2025), [arXiv:2506.21318 \[quant-ph\]](#).

[39] Z. Ding, Y. Zhan, J. Preskill, and L. Lin, [End-to-end efficient quantum thermal and ground state preparation made simple](#) (2025), [arXiv:2508.05703 \[quant-ph\]](#).

[40] L. Lin, Dissipative preparation of many-body quantum states: Toward practical quantum advantage, [APL Computational Physics](#) **1**, 10.1063/5.0283315 (2025).

[41] X. Mi, A. A. Michailidis, S. Shabani, K. C. Miao, P. V. Klimov, J. Lloyd, E. Rosenberg, R. Acharya, I. Aleiner, T. I. Andersen, M. Ansmann, F. Arute, K. Arya, A. Asfaw, J. Atalaya, J. C. Bardin, A. Bengtsson, G. Bortoli, A. Bourassa, J. Bovaard, L. Brill, M. Broughton, B. B. Buckley, D. A. Buell, T. Burger, B. Burkett, N. Bushnell, Z. Chen, B. Chiaro, D. Chik, C. Chou, J. Cogan, R. Collins, P. Conner, W. Courtney, A. L. Crook, B. Curtin, A. G. Dau, D. M. Debroy, A. Del Toro Barba, S. Demura, A. Di Paolo, I. K. Drozdov, A. Dunsworth, C. Erickson, L. Faoro, E. Farhi, R. Fatemi, V. S. Ferreira, L. F. Burgos, E. Fo-
rati, A. G. Fowler, B. Foxen, É. Genois, W. Giang, C. Gidney, D. Gilboa, M. Giustina, R. Gosula, J. A. Gross, S. Habegger, M. C. Hamilton, M. Hansen, M. P. Harrigan, S. D. Harrington, P. Heu, M. R. Hoffmann, S. Hong, T. Huang, A. Huff, W. J. Huggins, L. B. Ioffe, S. V. Isakov, J. Iveland, E. Jeffrey, Z. Jiang, C. Jones, P. Juhas, D. Kafri, K. Kechedzhi, T. Khat-
tar, M. Khezri, M. Kieferová, S. Kim, A. Kitaev, A. R. Klots, A. N. Korotkov, F. Kostritsa, J. M. Kreikebaum, D. Landhuis, P. Laptev, K. M. Lau, L. Laws, J. Lee, K. W. Lee, Y. D. Lensky, B. J. Lester, A. T. Lill, W. Liu, A. Locharla, F. D. Malone, O. Martin, J. R. McClean, M. McEwen, A. Mieszala, S. Montazeri, A. Morvan, R. Movassagh, W. Mruczkiewicz, M. Neeley, C. Neill, A. Nersisyan, M. Newman, J. H. Ng, A. Nguyen, M. Nguyen, M. Y. Niu, T. E. O'Brien, A. Opremcak, A. Petukhov, R. Potter, L. P. Pryadko, C. Quintana, C. Rocque, N. C. Rubin, N. Saei, D. Sank, K. Sankaragomathi, K. J. Satzinger, H. F. Schurkus, C. Schuster, M. J. Shearn, A. Shorter, N. Shutty, V. Shvarts, J. Skrzyni, W. C. Smith, R. Somma, G. Sterling, D. Strain, M. Szalay, A. Torres, G. Vidal, B. Villalonga, C. V. Heidweiller, T. White, B. W. K. Woo, C. Xing, Z. J. Yao, P. Yeh, J. Yoo, G. Young, A. Zalcman, Y. Zhang, N. Zhu, N. Zobrist, H. Neven, R. Babbush, D. Bacon, S. Boixo, J. Hilton, E. Lucero, A. Megrant, J. Kelly, Y. Chen, P. Roushan, V. Smelyanskiy, and D. A. Abanin, Stable quantum-correlated many-body states through engineered dissipation, [Science](#) **383**, 1332 (2024).

[42] Z. Ding, C.-F. Chen, and L. Lin, Single-ancilla ground state preparation via lindbladians, [Phys. Rev. Res.](#) **6**, 033147 (2024).

[43] https://docs.quantinuum.com/systems/user_guide/hardware.user_guide/performance_validation.html, accessed on January 13th, 2026.

[44] Y. Zhan, Z. Ding, J. Huhn, J. Gray, J. Preskill, G. K.-L. Chan, and L. Lin, [Rapid quantum ground state preparation via dissipative dynamics](#) (2025), [arXiv:2503.15827 \[quant-ph\]](#).

[45] D. Fang, J. Lu, and Y. Tong, Mixing time of open quantum systems via hypocoercivity, [Phys. Rev. Lett.](#) **134**, 140405 (2025).

[46] The experiments were conducted in June 2025 and November 2025.

[47] S. Sivarajah, S. Dilkes, A. Cowtan, W. Simmons, A. Edgington, and R. Duncan, $t\text{--ket}\rangle$: a retargetable compiler for nisq devices, [Quantum Science and Technology](#) **6**, 014003 (2020).

[48] A. Javadi-Abhari, M. Treinish, K. Krsulich, C. J. Wood, J. Lishman, J. Gacon, S. Martiel, P. D. Nation, L. S. Bishop, A. W. Cross, B. R. Johnson, and J. M. Gambetta, [Quantum computing with qiskit](#) (2024), [arXiv:2405.08810 \[quant-ph\]](#).

[49] S. Sivarajah, S. Dilkes, A. Cowtan, W. Simmons, A. Edgington, and R. Duncan, $t\text{--ket}\rangle$: a retargetable compiler for nisq devices, [Quantum Science and Technology](#) **6**, 014003 (2020).

[50] M. J. S. Beach, R. G. Melko, T. Grover, and T. H. Hsieh, Making trotters sprint: A variational imaginary time ansatz for quantum many-body systems, [Phys. Rev. B](#) **100**, 094434 (2019).

[51] H. Ezawa, Y. Tomozawa, and H. Umezawa, Quantum statistics of fields and multiple production of mesons, [Il Nuovo Cimento \(1955-1965\)](#) **5**, 810 (1957).